# Microglia-astrocyte interplay mitigates Aβ toxicity in a novel human 3D neurosphere model of Alzheimer's Disease

Stefan Wendt[1], Ada J. Lin[2], Sarah N. Ebert[1,4], Declan J. Brennan[2], Wenji Cai[2], Yanyang Bai[1], Stefano Sorrentino[2], Christopher J. Groten[1], Christopher Lee[2], Jonathan Frew[2,5], Hyun B. Choi[1], Konstantina Karamboulas[6], Mathias Delhaye[1], David R. Kaplan[3,6,7], Freda Miller[3,4], Brian A. MacVicar[1] and Haakon B. Nygaard[2]

[1] Department of Psychiatry, Djavad Mowafaghian Centre for Brain Health, University of British Columbia, Vancouver, V6T 1Z3, Canada.
[2] Division of Neurology, Djavad Mowafaghian Centre for Brain Health, University of British Columbia, Vancouver, V6T 1Z3, Canada.
[3] Department of Medical Genetics, University of British Columbia, Vancouver, V6T 1Z3, Canada.
[4] Michael Smith Laboratories, University of British Columbia, Vancouver, BC V6T 1Z4, Canada.
[5] Opalia Co., Montreal, QC H2X 3Y7 Canada
[6] Program in Neurosciences and Mental Health, Hospital for Sick Children, Toronto, ON M5G 0A4, Canada
[7] Department of Molecular Genetics, University of Toronto, Toronto, ON M5S 1A8, Canada

## Abstract

Microgliosis and astrogliosis characteristically occur at Aβ plaques in the brains of Alzheimer's disease (AD) patients although the impact of gliosis in AD is poorly understood. We studied the impact of Aβ-induced gliosis using human induced pluripotent stem cell (hiPSC)-derived 3D neurospheres (hiNS), containing only astrocytes and neurons versus hiNS with the addition of iPSC-derived microglia (hiMG). Applying Aβ to hiNS containing only astrocytes and neurons triggered pathological features of AD including plaque-like aggregates, reactive astrocytes, oxidative stress, neuronal dysfunction and cell death. In contrast, when hiMG were combined with hiNS, infiltrating hiMG effectively phagocytose Aβ and facilitate neuroprotection. Our findings further support a pivotal role for microglia in modulating astrocyte Aβ responses by inducing AD-associated gene expression in astrocytes, including the upregulation of *APOE*, crucial for Aβ clearance. This model, highlighting the neuroprotective potential of microglia-astrocyte interactions, offers a novel platform for exploring AD mechanisms and novel therapeutic strategies.

## *Highlights*

- The study utilized reproducible human iPSC-derived neurospheres (hiNS) consisting of neurons and astrocytes alone or with the addition of microglia/macrophages (hiMG)
- Chronic Aβ treatment mimicked neurodegeneration by triggering Aβ plaque-like aggregates, dysfunctional neuronal activity, glia activation, oxidative stress, and extensive neuronal death
- Aβ induced neurotoxicity was prevented by hiMG in a time-dependent manner
- hiMG efficiently phagocytose Aβ in hiNS
- Adding hiMG during Aβ exposure induced changes in astrocyte gene expression that were similar to changes observed in human AD such as the induction of APOE expression

## Introduction

Alzheimer's disease (AD) remains inextricably linked to progressive aggregation of Aβ and tau in the brain. Both are prime targets for therapeutic interventions, with two monoclonal antibodies against Aβ recently approved by the US Food and Drug Administration for use in AD. The mechanisms by which Aβ and tau cause neurodegeneration remain incompletely understood. Aβ plaques initiates a significant neuroinflammatory reaction including robust microglial activation. Whether this activation is detrimental, neuroprotective, or both, remains controversial. A mutation in TREM2, which impacts the efficiency with which microglia phagocytose Aβ, confers significant risk for developing sporadic AD, suggestive an important protective role of microglia[1]. Microglial phagocytosis is also the principal mechanism by which the monoclonal antibodies against Aβ, such as lecanemab, remove brain Aβ, leading to improvement in clinical function and AD biomarkers[2,3]. However, in preclinical models, microglial activation can also lead to excessive synaptic pruning which could accelerate neurodegeneration[4]. Recent genomic analysis of sporadic AD has linked numerous genes of interest, such as *APOE,* to glial cells[5], further emphasizing the potential importance of glia in sporadic AD pathophysiology[6-8]

The development of physiologically relevant human models of AD is critical for discovering and defining potential therapeutic targets. While murine models of AD have been used to investigate cellular mechanisms in AD, clinical trials based on results from murine AD models, were rarely successful[9]. The establishment of cerebral organoid and neurosphere 3D human cell culture systems sparked widespread interest in developing 3D cell culture models that more faithfully resemble human AD, to achieve better translation of pre-clinical studies to novel therapies[10-13]. Many of these approaches rely on the expression of familial AD mutations in *APP* or *PSEN1*[14-17]. Mimicking the AD-associated transcriptional changes of glial cells in a human 3D sporadic AD model system could help to unravel the impact of neuron-glia-Aβ interactions in AD.

Here we investigated the utility of using human induced pluripotent stem cell (hiPSC)-derived 3D neurospheres (hiNS) to determine the impact of chronic amyloidosis, a characteristic feature of AD, on neuronal and glial function. The introduction of hiPSC-derived microglia (hiMG) into hiNS during chronic Aβ treatment triggered striking neuroprotection, by preventing Aβ-induced dysfunction of neuronal activity, oxidative stress and reducing neuronal death. While hiMG displayed a remarkable phagocytic activity towards Aβ, single nuclei RNA sequencing revealed that the addition of hiMG also had particularly dramatic effects on astrocyte transcriptional profiles. For example, many AD-associated genes of interest in astrocytes, such as *APOE*, *CLU*, *LRP1* and *VIM*, were upregulated only in the presence of hiMG, implying a shift in astrocytes towards enhanced neuroprotection. This study sheds light on the critical timing and multifaceted role of microglia and astrocyte neuroprotection, offering new insights into potential therapeutic strategies for AD.

## Results

### Formation of hiPSC-derived neurospheres (hiNS) as a 3D tissue culture system includes functional neurons, astrocytes and microglia (hiMG)

Blood-derived hiPSCs were generated from a healthy individual and subsequently differentiated into neural progenitor cells (NPCs) (Suppl. Table 1). NPCs were plated in an AggreWell™ 800 plate to initiate the formation of hiNS. After 7 days *in vitro* (DIV), hiNS were transferred to 10 cm petri dishes on an orbital shaker for subsequent differentiation and maturation before plating into

48-well plates. While NPCs differentiated into neurons and astrocytes spontaneously, microglia did not differentiate in the 3D neurospheres. Therefore, hiMG were cultured in parallel to hiNS and were added to a subset of mature neurospheres with neurons and astrocytes/NPCs to determine the impact of microglia. Neurospheres in which hiMG were not added are termed hiNS(-) whereas neurospheres after hiMG infiltration are termed hiNS(+) (Figure 1A). hiNS were readily transduced using adeno associated viruses (AAVs) encoding cell type specific expression with the neuronal-selective promoter *hSyn* or the astrocytes-selective promoter *gfaABC1D*. While cerebral organoids are commonly used, their large size often leads to severe necrosis within the central regions of the tissue[18]. Our hiNS did not develop necrotic regions, likely because they remain a smaller size, rarely exceeding a diameter of 500 μm. To monitor tissue health of hiNS, we transduced neurospheres with *hSyn*-roGFP1, a redox-sensitive green fluorescent protein that detects cellular oxidative stress associated with reactive oxygen species production and typically, necrosis[19,20]. As controls, DTT (5 mM) was used to fully reduce neurospheres and diamide (2 mM) to fully oxidize the tissue. We found that neurons in hiNS displayed a largely reduced cytosol throughout the neurosphere, confirming the absence of necrotic tissue (N = 4 each, Figure 1B).

To confirm the identity of cell types in hiNS, we performed single nuclei RNA sequencing (snRNA-seq). Specifically, we cultured hiNS for 50 days, and hiMG were added and allowed to infiltrate into the tissue for another 10 days. hiNS(+) or hiNS(-) were collected and flash frozen for subsequent snRNA-seq analysis. Single cell nuclei were isolated and sequenced using the 10X Genomics platform. Transcriptome analysis was performed using our previously described pipeline[21-25]. After filtering the datasets for low quality cells with few expressed genes or high mitochondrial proportions and cell doublets, we obtained 4750 and 1892 single cell transcriptomes for the hiNS(+) and hiNS(-), respectively. We then merged the datasets to allow a direct comparison of transcriptomes in the two conditions. Genes with high variance were used to compute principal components as inputs for projecting cells in two-dimensions using t-distributed stochastic neighbor embedding (t-SNE) and clustering performed using a shared nearest neighbors-cliq (SNN-cliq)-inspired approach built into the Seurat R package at a range of resolutions.

Uniform Manifold Approximation and Projection for Dimension Reduction (UMAP) visualization and analysis of well-defined marker genes identified 15 clusters containing the predicted cell types (Figure 1C,D). Cell clusters with similar gene expressions were grouped together in a two-dimensional UMAP. This included astrocytes expressing *GFAP, AQP4, SLC1A3* and *GABBR2* (cluster 0), and two types of neurons in various stages of maturation: inhibitory interneurons (clusters 4, 7, 9 and 14) expressing *GAD1, GAD2* and *SYN3*, and excitatory neurons (clusters 2,3,5,6,11,12 and 15) enriched for *GRID2, GRM7, SLC17A6* and *SYN3*. The dataset also included neural precursor cells (clusters 1, 10 and 14), and microglia/macrophages expressing *PTPRC, AIF1, CX3CR1* and *CD68* (cluster 13). Note that *GFAP* expression was not exclusive to astrocytes but also highly expressed in some neural precursor populations.

Analysis of the dataset of origin (Figure 1E) confirmed that the microglial cluster included cells only from the hiNS(+) dataset. The other clusters included intermingled cells from both conditions, except for cluster 0 astrocytes, where many of the cells appeared transcriptionally distinct. To further explore this finding, we subsetted the astrocytes and reanalyzed them separately. This analysis (Figure 1F,G) defined two large clusters and one smaller cluster. Two of the clusters (0a and 0c) included astrocytes from both conditions, while the other large cluster (0b) was almost completely comprised of hiNS(+) astrocytes. Pearson correlation analysis of average gene

expression confirmed that, as suggested by the clustering analysis, hiNS(+) astrocytes were similar but not identical to the hiNS(-) astrocytes, with r = 0.978 (Figure 1H).

To better understand these similarities and differences, we performed differential gene expression (DEG) analysis. There were 663 DEGs when comparing the two conditions, with 394 enriched in hiNS(+) astrocytes and 269 in hiNS(-) astrocytes (> 1.4-fold average change, p adj < 0.05; Suppl. Tables 2 and 3). Notably, DEG analysis coupled with gene ontology (Figure 1I,J; Suppl. Table 4) demonstrated that hiNS(+) astrocytes were highly enriched for genes and gene categories associated with oxidative phosphorylation such as *MT-CO3, MT-ND3*, *MT-ATP6,* and *MT-CYB*, suggesting they were more metabolically active. By contrast, hiNS(-) astrocytes gene ontology analysis identified only a few highly significant gene categories including nervous system development and post-synapse (Figure 1J, Suppl. Table 5).

To confirm the presence of our major cell populations from our snRNA-seq analysis, we performed immunofluorescence for neurons (MAP2), astrocytes/NPCs (GFAP), and microglia/macrophages (IBA1) in fixed hiNS(+) at DIV 60. Indeed, highly processed neuronal and astrocytic cells formed tight networks throughout the tissue with hiMG populating the 3D space (Figure 2A). Neuronal activity in hiNS was monitored by inducing *hSyn*-GCaMP6f expression for live imaging of neuronal intracellular calcium concentration $[Ca^{2+}]_i$ transients. Induction of *hSyn*-iGluSnFr expression in neurons was used for imaging of extracellular glutamate release. hiNS(-) displayed frequent calcium transients and glutamate release in a synchronized manner (Figure 2B). Due to the superior signal-to-noise ratio of GCaMP6f over iGluSnFr we used imaging of $[Ca^{2+}]_i$ transients to quantify neuronal activity. The synchronized large $[Ca^{2+}]_i$ transients traversed through hiNS in a wave-like pattern reminiscence of large calcium waves (Figure 2C) observed during neurodevelopment[26,27]. Calcium waves were suppressed by the $Na^+$ channel blockers TTX and the ionotropic glutamate receptor antagonists AP5/CNQX, and by GABA treatment. Picrotoxin application, which antagonizes GABA receptors and chloride channels, significantly increased calcium wave frequencies (Figure 2D). We then tested whether infiltrating hiMG alter calcium wave frequencies by comparing GCaMP6f recordings from hiNS(-) (N = 10) with hiNS(+) (N = 12). The presence of hiMG reduced the calcium wave frequency by half from 0.19 to 0.09 Hz (*** p<0.001) and increased wave duration from 3.2 to 5.0 sec (** p<0.01) indicating that hiMG leads to altered neuronal activity or neurodevelopment (Figure 2E).

We next investigated the infiltration behaviour and physiological properties of hiMG during and after tissue infiltration into hiNS. hiMGs were identified after fixation by IBA1 immunofluorescence or were live-stained using tomato lectin conjugated dyes (Figure S1). We performed 24h-continuous confocal live imaging on hiNS expressing *hSyn*-mCherry and *gfaABC1D*-EGFP to monitor live-stained hiMG infiltrating into hiNS (N = 4). hiMG were pre-stained with tomato lectin DyLight 649. Tracking hiMG movements in hiNS revealed infiltration occurring 6-12h after the transfer (see yellow arrows, Figure 2F). To test if hiMG that infiltrated within hiNS(+) exhibit physiological microglia-like properties, we again stained hiMG with tomato lectin (DyLight 488) 7-9 days post-infiltration into hiNS. hiNS(+) were imaged by 2-photon microscopy to monitor microglial process movement, damage responses and for patch-clamp recordings. We observed tissue surveillance by hiMG processes as well as a robust process outgrowth towards a focal laser lesion mimicking *in vivo*-like behaviour (N=3, Figure 2G). Patch-clamp recordings on hiMG within hiNS(+) confirmed microglial identity, revealing average reversal potentials of -38 ± 3.9 mV and cell capacitances of 22 ± 2.4 pF (N = 9). A series of de- and hyperpolarizing voltage steps revealed inward rectifying potassium currents typical for microglia[28-30] (Figure 2H). We conclude

175 that infiltrating hiMG display a robust microglial-like phenotype exhibiting several properties that
176 resemble *in vivo* microglia.

177 **Chronic treatment of hiNS with oligomeric Aβ results in plaque-like aggregates and a series**
178 **of neurotoxic effects mimicking severe amyloidosis**

179 To model amyloidosis and AD neurodegeneration, we tested the impact of supplementing hiNS(-
180 ) media with oligomeric Aβ42 (0.24 μg/mL) for up to 35 days, first in the absence of hiMG (Figure
181 3A). Chronic Aβ treatment results in extracellular plaque-like aggregates within hiNS(-) (Figure
182 3B). Immunostaining for neurons and astrocytes/NPCs revealed dystrophic processes and cell
183 bodies at the end of the treatment period indicating neurotoxicity (Figure 3C, see arrows). To
184 monitor neuronal redox levels, hiNS(-) expressing *hSyn*-roGFP1 were imaged after treatment,
185 revealing severe oxidative stress evident by a significant increase in roGFP redox ratio (green
186 emission acquired at 405nm divided by green emission acquired at 488 nm) (Figure 3D).
187 Continuous (up to 20h) live roGFP1 imaging in Aβ treated hiNS revealed a significant increase in
188 the frequency of oxidizing cells compared to hiNS not exposed to Aβ, further confirming Aβ-
189 induced oxidative stress (Figure S2). Neuronal activity was repeatedly monitored by imaging
190 GCaMP6f in hiNS(-) as described above. A significant reduction in calcium wave frequencies was
191 observed at the end of the third week and in the fourth week of Aβ exposure (Figure 3E).

192 We then investigated whether chronic Aβ treatment ultimately results in neuronal loss.
193 Immunostaining for cleaved Caspase-3 (c-Cas-3), a key mediator of neuronal apoptosis, indicated
194 a 50% increase in apoptotic cells after Aβ treatment in hiNS(-) as well as a significant reduction
195 of nuclei density within the tissue, suggesting cell death (Figure 3F). Neuronal apoptosis during
196 Aβ exposure was observed by co-staining for c-Cas-3 and the neuronal marker MAP2 (Figure
197 3G). To confirm the increase in apoptotic cell death, we performed terminal deoxynucleotidyl
198 transferase dUTP nick end labeling (TUNEL) to detect fragmented DNA. There was a significant
199 increase in TUNEL fluorescence confirming apoptosis during chronic Aβ exposure (Figure 3H). In
200 conclusion, our chronic Aβ stimulation protocol resulted in a sequence of neurotoxic effects
201 including the formation of plaque-like Aβ aggregates within days of exposure, oxidative stress and
202 dysfunctional neuronal activity 3-4 weeks into Aβ treatment and ultimately Caspase-3 dependent
203 apoptosis and neuronal loss 4-5 weeks after Aβ exposure, mimicking key hallmarks of AD.

204 **Time-dependent neuroprotective properties of hiMG during chronic Aβ stimulation**

205 The role of microglia in AD pathogenesis has been extensively studied, with both neurotoxic- and
206 neuroprotective roles described[31,32]. We designed two different chronic Aβ treatment protocols
207 that included six experimental conditions: control (ctrl), 3-week (3w Aβ hiNS) or 5-week (5w Aβ
208 hiNS) exposure each with (+) or without (-) hiMG. hiMG were added to the tissue for the last 10
209 days of the treatment protocol to test the impact of microglia on Aβ induced neurotoxicity after
210 either a mild (3w Aβ) or severe (5w Aβ) chronic treatment (Figure 4A). Visual inspection revealed
211 hiMG attached to and accumulate around hiNS prior to infiltration, and 5w Aβ treated hiNS
212 displayed morphological changes indicating tissue degeneration (Figure S3). We quantified Aβ
213 immunoreactivity using anti-Aβ (4G8) for all groups. As expected, the amount of Aβ was less at
214 3w Aβ compared to 5w Aβ. hiMG addition significantly reduced extracellular Aβ levels at 3w and
215 not at 5w, indicating that adding hiMG are more efficient at Aβ aggregate clearance during the
216 shorter Aβ treatment protocol. Analysis of soluble Aβ levels using ELISA, however, showed a

reduction in 5w hiNS(+), suggesting active phagocytosis but without a noticeable reduction in extracellular aggregates (Figure 4B).

We investigated whether hiMG phagocytosis of Aβ contributed to the observed reduction in Aβ deposits and soluble Aβ. Co-staining microglia (lectin or IBA1) and Aβ (6E10, 4G8 or mOC87) revealed that Aβ was readily found in the cytosol of infiltrated hiMG in Aβ treated hiNS (Figure S4A). The strongest intracellular Aβ was seen by staining specifically for fibrillar Aβ (mOC87[33]), while the Aβ antibody clone 6E10 revealed only a faint signal inside hiMG, indicating that Aβ inside hiMG appears mostly in a highly aggregated form. Intracellular Aβ was identified after both 3w and 5w Aβ treatment (Figure S4B, white arrows). While we did not find microglia to significantly reduce overall extracellular Aβ burden after 5w, microglia appear to have cleared noticeable amounts of Aβ, leaving Aβ–cleared tissue in their path (Figure S4B, red arrows) which were absent in 3w Aβ cultures.

Successful phagocytosis requires the uptake of Aβ into acidic phagocytic compartments. We conjugated our oligomeric Aβ with pHrodo green which is fluorescent at acidic pH[34]. hiNS were treated with regular oligomeric Aβ for 3w followed by pHrodo-Aβ for an additional 7 days (4w Aβ total). Aβ treatment was then stopped prior to hiMG addition. hiNS were fixed 8 days later and imaged to quantify intracellular pHrodo-Aβ levels in the tissue. We found a strong uptake of pHrodo-Aβ inside IBA1 positive hiMG, whereas only small amounts overlapped with GFAP-positive astrocytes/NPCs, confirming that the main cell type in hiNS(+) facilitating Aβ phagocytosis were microglial cells (Figure S4C).

We then immunostained for neurons (MAP2), astrocytes/NPCs (GFAP), and microglia (IBA1) markers in all six experimental conditions. First, we quantified the number of hiMG infiltrating into hiNS and found that the number of hiMG within 5w Aβ hiNS(+) increased by more than two-fold compared to ctrl hiNS(+), whereas the number of microglia in 3w Aβ hiNS(+) did not increase. Additionally, we found that GFAP immunofluorescence increased significantly in the presence of hiMG at 3w and 5w indicating microglial-dependent astrocyte reactivity by Aβ (Figure 4C). We repeated our roGFP redox imaging (here fixed, following 4% PFA + 20 mM N-Ethylmaleimide incubation at DIV 60) and found that 3w Aβ exposure in hiNS(-) resulted in mild, but highly significant (***, $p<0.001$), oxidative stress which was completely inhibited by the presence of hiMG, suggesting neuroprotective functions of microglia (Figure 4D, upper part). However, Aβ induced oxidative stress at 5w was severe and not significantly reduced after hiMG infiltration (Figure 4D, bottom). We monitored neuronal activity using GCaMP6f and found that calcium wave frequencies were reduced in 3w Aβ hiNS(-), while microglia fully rescued neuronal activity in 3w Aβ hiNS(+) (**, $p<0.01$), confirming their neuroprotective ability. At 5w Aβ, calcium waves were completely absent without ameliorating effects of hiMG, suggesting that functional recovery is only possible if hiMG are present relatively early during chronic Aβ treatment (Figure 4E).

We then determined whether hiMG prevented neuronal death by staining for c-Cas-3 and quantifying nuclei in hiNS. While we found only a moderate increase in c-Cas-3 immunoreactivity at 3w, it was significantly reduced in 3w Aβ hiNS(+). We found a significant loss of cells when comparing the nuclei density of ctrl hiNS(-) with 3w Aβ hiNS(-) (*, $p = 0.03$), while the differences of ctrl vs 3w Aβ hiNS(+) were not significant ($p =0.35$). Note that hiMG were identified by lectin staining, and their nuclei count was subtracted from whole-tissue nuclei quantification. At 5w Aβ, c-Cas-3 immunoreactivity was highest in hiNS(-), with a significant reduction in 5w Aβ hiNS(+).

Cell density in 5w Aβ hiNS(-) was dramatically reduced and partially but highly significantly rescued in 5w Aβ hiNS(+) (***, $p<0.001$) (Figure 4F).

We further investigated the electrophysiological properties of hiMG in Aβ treated hiNS. Membrane capacitances were significantly increased at 5w Aβ (Figure S5), but no other changes were significant. These data indicate that the neuroprotective potential of hiMG during chronic Aβ exposure is highly time-dependent: At 3w Aβ, added hiMG preserved neuronal function, preventing oxidative stress, and reducing Caspase-3 cleavage. While at 5w Aβ, hiMG did not rescue neuronal function or reduce oxidative stress but significantly reduce apoptosis and loss of cell nuclei, demonstrating limited neuroprotective properties at late stages of amyloidosis.

To better understand the phenotypical changes of hiMG during chronic Aβ treatment, we analyzed cell culture supernatant of the above hiNS conditions for proinflammatory cytokine levels using a multiplex ELISA. Supernatant was collected on the last day of the treatment protocol. Overall, cytokine levels were enriched in media of all hiNS(+) samples but not in hiNS(-), indicating that hiMG produce the listed cytokines independent of Aβ exposure. Note that IL-8 data was excluded from the panel due to saturated readings for hiNS(+) groups, preventing accurate quantification. Interestingly, only IL-6 and IL-12 levels increased significantly (** $p<0.01$) with 5w Aβ treatment, indicating an Aβ induced shift in hiMG cytokine production (Figure 4G). Note that classical markers for proinflammatory microglia, such as IL1β and TNFα were not increased in 3w/5w Aβ hiNS(+).

**Expression of subsets of astrocyte marker genes for AD depends on the presence of hiMG**

We performed snRNA-seq on all six hiNS culture conditions (ctrl, 3w Aβ, 5w Aβ with or without hiMG). We isolated and sequenced single cell nuclei using the 10X Genomics platform and put the resultant transcriptomes through our pipeline[21-25]. After filtering the datasets for low quality cells, we merged these transcriptomes with those of the previously analyzed control hiNS (as in Figure. 1C,E).

UMAP visualization and analysis of the datasets of origin showed that the datasets merged well (Figure 5A,B). Marker gene analysis defined all of the same cell types that were seen in the control hiNS cultures including neural and glial precursor cells, astrocytes, inhibitory and excitatory neuron lineages, and microglia/macrophages. However, analysis of the datasets of origin identified differences in cellular composition that were most obvious in the 5w Aβ hiNS. Specifically, in the 5w Aβ hiNS(-), the only surviving cells were astrocytes and inhibitory neurons, while excitatory neurons were almost entirely absent which is consistent with the reduction of nuclei numbers in this group (Figure 4F). The 5w Aβ hiNS(+) did contain some excitatory and inhibitory neurons, but these were reduced relative to the 3w Aβ cultures and control groups. In addition, relative to the ctrl and 3w Aβ hiNS (+), there were proportionately more hiMG in 5w Aβ hiNS(+), likely reflecting increased proliferation or infiltration of microglia matching our hiMG quantification (Figure 4C). By contrast, the distribution of cell types in the 3w Aβ hiNS cultures was similar to that seen in the control groups.

We next compared astrocytes in these different culture conditions by subsetting and reanalyzing transcriptomes from cluster 0. UMAP cluster and dataset of origin visualizations (Figure 5C,D) identified four clusters containing variable proportions of astrocytes from the different culture conditions. In particular, most astrocytes that came from cultures without added microglia were

302 localized to cluster 0b regardless of whether they were exposed to control peptide or Aβ.
303 Conversely, most astrocytes from cultures with hiMG were localized to cluster 0a. The exceptions
304 to this intermingling were cluster 0d, which was almost completely comprised of transcriptomes
305 from the 5w Aβ hiNS(+) cultures, and cluster 0c, which was comprised of astrocytes from the
306 control hiNS(+) cultures (Figure 5E).

307 These data suggest that astrocytes in the different cultures were transcriptionally distinct. We
308 therefore assessed how Aβ altered astrocytes in the presence of hiMG by performing DEG
309 analysis comparing the 5w Aβ hiNS(+) cells with ctrl hiNS(+). This analysis identified 288 DEGs
310 when comparing the two conditions, with 174 enriched in 5w Aβ hiNS+ cells and 114 in ctrl hiNS(+)
311 without Aβ (> 1.4-fold average change, p adj < 0.05; Suppl. Tables 6 and 7). Single-cell gene
312 expression heatmaps (Figure 5F) showed that only a few of these mRNAs were upregulated in
313 the 3w Aβ hiNS(+) astrocytes, and required exposure to both Aβ for 5w and the presence of hiMG
314 before seeing a significant change in mRNA expression. Notably, gene expression overlays
315 showed some of the most highly upregulated genes following Aβ exposure are known to be
316 associated with the astrocyte response in AD, including *APOE, CLU, SPP1, TLR4, VIM, S100A11*
317 and *LRP1* (Figure 5G). Notably, gene ontology comparing mRNAs upregulated in 5w Aβ hiNS(+)
318 relative to ctrl hiNS(+) astrocytes (Suppl. Table 8) showed that the top-ranked term in the
319 molecular function category was Aβ binding (Figure 5H). By contrast, genes that were significantly
320 decreased in 5w Aβ hiNS(+) astrocytes were highly associated with gene ontology terms like
321 nervous system development and postsynaptic membrane (Suppl. Table 9), suggesting that the
322 presence of Aβ interferes with normal astrocyte biology and cellular interactions.

323 Next, we compared astrocytes of 3w and 5w Aβ directly with or without hiMG addition and plotted
324 the results in volcano plots (Figure 5I). Again, the expression of AD-associated astrocyte genes
325 depends on the presence of hiMG during Aβ exposure, including genes such as *GFAP*, *APOE*,
326 and *VIM.* Interestingly, we found DEGs linked to oxidative stress handling (*OXR1*, *CCL2* and
327 *CHL1*) to be upregulated only in 3w Aβ hiNS(+), the experimental group in which we observed a
328 significant reduction in Aβ induced oxidative stress (Figure 4D). Thus, in hiNS(+) exposed to Aβ
329 for 3 weeks, hiMG increase the expression of subsets of astrocyte marker genes associated with
330 AD as well as the expression of genes handling oxidative stress.

331 **Chronic Aβ treatment results in heterogenous gene expression profiles in hiMG**

332 After characterizing the shift in astrocyte gene expression by hiMG during chronic Aβ exposure
333 we subsetted the microglia/macrophages (cluster 13, Figure 5A) of the 5w Aβ hiNS(+)
334 experimental group to investigate gene expression profiles in hiMG to better understand their
335 reactive state. We identified 3 distinct clusters within the microglia/macrophage group which we
336 identified further by DEG analysis (Figure 6A). Cluster 13a showed similarities to a more
337 macrophage-like population characterized by upregulation of *CD36*, *TLR2*, *SYK*, *SLC11A1* and
338 *PTPRC.* Cluster 13c mimics gene expression of homeostatic microglia-like cells including
339 upregulation of *ITGAM*, *CX3CR1* and *P2RY12*. Cluster 13b gene expression was similar to a
340 disease associated microglia (DAM)[35]-like state, sharing a large number of DEGs including
341 *APOE*, *TREM2*, *CD9*, *LPL*, *CD9* and *B2M,* indicating that chronic Aβ exposure induces a similar
342 activation state in a subset of hiMG in 5w Aβ hiNS(+) (Figure 6B). We conclude that the
343 microglia/macrophage population in Aβ treated hiNS(+) is heterogeneous and that each
344 subpopulation could play distinct pathophysiological roles. We performed gene ontology analysis

345 on all three clusters highlighting distinct biological processes of each individual group (Figure 6C).
346 Volcano plots highlighting DEGs genes of interest for each sub-cluster displayed in Figure 6D
347 (see heatmap with most significant DEGs in Figure S6).

348 **APOE expression in Aβ treated hiNS is hiMG-dependent**

349 *APOE* is well known for being the most important genetic risk factor for sporadic AD and its role
350 in amyloid clearance[36]. The iPSC-line used in this study carries the common homozygous ε3 allele
351 thought to be 'neutral' without increasing or decreasing AD risk. We found astrocytic *APOE*
352 expression to be upregulated in 5w Aβ hiNS(+) (Figure 5F,G) as well as in a subset of hiMG
353 (Figure 6B,D) from the same treatment group. We next immunostained for APOE in fixed slices
354 (80 μm) of hiNS of all six experimental groups and found significant increases in immunoreactivity
355 exclusively in 3w/5w Aβ hiNS(+), indicating that high expression of APOE appears only in Aβ-
356 treated hiNS that also contain hiMG (Figure 7A,B). Next, we investigated if APOE is present
357 intracellularly in hiMG and/or astrocytes by co-staining for IBA1 and GFAP. We observed APOE-
358 positive hiMG whereas APOE-positive astrocytes were less frequent (Figure 7C). Additional co-
359 staining for APOE and Aβ (4G8) of 5w Aβ hiNS(-/+) confirmed that extracellular APOE aggregates
360 co-localized with extracellular Aβ at the outer tissue volumes of hiNS in a microglia-dependent
361 manner (Figure 7D). We then examined APOE expression patterns in human post-mortem AD
362 brain sections to validate our APOE expression data in our AD neurosphere model. To remove
363 background and autofluorescence of paraffin-embedded human cryosections, we cleared and
364 expanded the tissue, based on a recently developed protocol[37] prior to immunofluorescence, and
365 stained sections from two familial AD as well as one sporadic AD patient. In all three patients, we
366 found APOE co-localized with dense-core Aβ plaques, while co-staining for GFAP revealed
367 APOE-positive astrocytes in AD patients (Figure 7E). In summary, our 5w Aβ hiNS(+)
368 experimental condition mimics key features of AD APOE expression, offering a novel tool to study
369 APOE function in microglia and/or astrocytes.

370 **Discussion**

371 **Functional characteristics of hiNS demonstrate healthy brain physiology**

372 Our protocol for the generation of hiNS relies on the differentiation of human iPSC-derived NPCs
373 into neuronal and astrocyte-like cell populations into a spherical 3D tissue culture model (Figure
374 1,2). We extensively characterized the physiological properties of hiNS and showed that neurons
375 in hiNS maintain a healthy reduced redox status with high levels of synchronized wave-like
376 neuronal activity, matching previous reports of calcium waves in both brain development[38,39] and
377 other neurosphere cultures[40,41]. Our pharmacological data suggest that both excitatory and
378 inhibitory neurons contribute to calcium wave formation and dynamics matching other
379 pharmacological studies[41]. During brain development, not only do neurons and astrocytes play
380 key roles, but infiltrating microglial cells into the brain are vital in shaping the neuronal network[42].
381 Few other studies[15,43] have incorporated microglia into neurospheres using different protocols
382 suggesting robust tissue infiltrating properties of iPSC-derived microglia/macrophages. hiMG
383 readily infiltrate hiNS attached to Matrigel-coated surfaces, and we demonstrate that hiMG display
384 microglia-like electrophysiological properties similar to mature *in situ* ramified mouse or human
385 microglia[28,30,44]. Moreover, we show that the presence of microglia shapes neuronal calcium wave
386 frequency and duration but also how they alter the transcriptional landscape of other cell types in
387 hiNS (Figure 1). Our gene expression analysis of astrocytes in hiNS with vs. without hiMG
388 revealed an increase of gene expression linked to mitochondrial function and oxidative

389 phosphorylation, indicating increased metabolic function in the presence of microglia. We believe
390 that our hiNS offer unique opportunities to investigate neuron-glia interaction in human brain
391 development.

392 **Chronic Aβ induced neurotoxicity in hiNS mimics hallmarks of AD pathology**

393 Instead of utilizing familial AD mutations in *APP* or *PS1* to drive Aβ pathology, we modeled chronic
394 amyloidosis by supplementing hiNS media with low concentrations of oligomeric Aβ (~0.24
395 μg/mL) for 3 to 5 weeks to induce transient and slow neurotoxicity (Figure 3). Accumulation of Aβ
396 in the brain of AD patients is believed to be one of the earliest pathological events, occurring
397 decades before dementia manifests[45]. We did not observe any pathological impact within the first
398 2 weeks of Aβ exposure in hiNS, even though Aβ aggregates can be detected in the tissue at that
399 point. However, at the end of 3-week long exposure to Aβ we found that calcium wave frequency
400 dropped and that oxidative stress became evident (Figure 3). Oxidative stress is a known early
401 hallmark of AD believed to precede the loss of neurons[46,47]. It can be observed by
402 immunofluorescence staining of post-mortem AD brain tissue[48]. Here we demonstrate how
403 chronic Aβ exposure over time leads to the build-up of oxidative stress in neurons, which precedes
404 the severe cell death observed after 4-5 weeks of Aβ treatment. Similarly, network dysfunction
405 and synaptic dysregulation[49] are early known features of AD pathogenesis are believed to
406 precede neurodegeneration and coincide with the formation of Aβ induced oxidative stress in
407 hiNS. Our immunofluorescence staining of hiNS after long Aβ exposure indicates an increase in
408 cleaved Casp-3 immunoreactivity and TUNEL fluorescence, implicating apoptosis as a key cell
409 death pathway. Although caspase-dependent cell death has been proposed as a neuronal death
410 pathway in AD[50,51], multiple other pathways have more recently been proposed to play a role in
411 later stages of disease progression[52]. More research is needed to decipher the exact cell death
412 pathways in our Aβ treated hiNS, but our model offers a slow-progressing pathology to study key
413 AD disease mechanisms in a human 3D tissue environment.

414 **Impact of hiMG on Aβ clearance and neurodegeneration**

415 While microglia have gained substantial attention in the field over the past 10 years, their precise
416 role in AD pathogenesis remains elusive[53-55]. During the initial stages of AD, microglia are
417 generally believed to release anti-inflammatory cytokines and neurotrophic factors, and are
418 efficient in phagocytosing Aβ; later in AD pathology microglia switch to producing pro-inflammatory
419 cytokines, actively contribute to neurodegeneration and have a reduced capacity to clear Aβ from
420 the brain[56-58]. We have demonstrated that hiMG, within a 10-day time window, prevent oxidative
421 stress and sustain neuronal calcium wave activity early during chronic Aβ treatment. When
422 introducing hiMG at a later stage, loss of neuronal activity or severe oxidative stress was not
423 recovered, but overall cell death in hiNS was markedly reduced, highlighting robust
424 neuroprotection (Figure 4D-F). Quantifying levels of a series of pro-inflammatory cytokines from
425 the supernatant of all treatment groups revealed that all measured cytokines were produced in all
426 hiNS(+) groups. However, typical pro-inflammatory cytokines, like IL1β and TNFα, were not
427 elevated in 3w/5w Aβ hiNS(+) when compared to ctrl hiNS(+). Indeed, we saw a robust release
428 of these cytokines (Figure S1) when hiMG were stimulated with LPS, which is known to induce
429 pro-inflammatory cytokine production[59]. We conclude that the production of cytokines in ctrl
430 hiNS(+) marks the baseline levels without indicating a pro-inflammatory phenotype. The only two
431 cytokines significantly increased with Aβ treatment were IL-6 and IL-12 (Figure 4G), which have
432 previously been reported to play either pro- or anti-inflammatory roles[60-64]. Defining the definite

433 roles of these cytokines should be addressed in future studies to shed light on which cytokines
434 have a clear neuroprotective function in our human AD model system. Levels of aggregated and
435 soluble Aβ were markedly reduced in 3w Aβ and 5w Aβ hiNS(+), respectively, strongly indicating
436 active phagocytic capacities of hiMG. Other groups have reported that human iPSC-derived
437 microglia are capable of phagocytosing Aβ[65,66]. We, therefore, conclude that hiMG acquired an
438 overall neuroprotective phenotype in our chronic Aβ model system.

439 Recently, Takata et al.[67] have demonstrated in a similar 3D cell culture model that the addition of
440 iPSC-derived primitive macrophages during Aβ treatment resulted in less Aβ aggregation and
441 better survival of neurons, indicating that this activation state of microglia-like cells is consistent
442 between similar model systems. Modelling interaction with peripheral immune cells is a possible
443 requirement to trigger robust pro-inflammatory phenotypes. Blood-brain-barrier (BBB) breakdown
444 leads to infiltration of soluble factors and cells from the periphery and is a known hallmark of AD
445 and linked to neuroinflammation[68], this process is not modelled in the current study. Most recently,
446 in an amyloid-overproducing 3D tissue culture model comprised of neurons, astrocytes and
447 microglia, the addition of peripheral immune cells, particularly $CD8^+$ T cells, greatly facilitated Aβ
448 induced neurodegeneration; although the addition of microglia alone appeared to have neurotoxic
449 effects[15], matching previous observations using the same model system[43]. It is therefore
450 reasonable to suggest that our hiMG could be polarized to a more neurotoxic function by further
451 modelling aspects of BBB breakdown or interaction with peripheral immune cells.

452 **Astrocyte AD-like activation state depends on hiMG-facilitating neuroprotection**

453 Our immunofluorescence staining revealed a dramatic increase in reactive microglia and GFAP
454 immunoreactivity in 5w Aβ hiNS(+), suggesting gliosis triggered by Aβ exposure (Figure 4C).
455 Reactive astrocytes are known to play both beneficial and detrimental roles in AD pathology[69]. To
456 understand the reactive state of astrocytes in our AD model system we performed snRNA-seq
457 analysis on Aβ treated hiNS with or without hiMG, comparing gene expression levels to control
458 hiNS. The size differences of identified cell populations in our merged data set confirmed our
459 immunohistochemical analysis. Firstly, hiMG populations were exclusive to hiNS(+) treatment
460 groups in which 5w Aβ hiNS(+) harbored far more microglia than ctrl and 3w Aβ hiNS(+). Secondly,
461 in the absence of hiMG, chronic Aβ treatment resulted in much lower cell counts, indicating severe
462 loss of excitatory neurons in 5w Aβ hiNS(-) (Figure 5B).

463 We found that the presence of hiMG shifted the transcriptional profile of the astrocyte cluster in
464 Aβ treated groups. Interestingly, 3w and 5w Aβ hiNS(+) astrocytes appeared to have unique
465 transcriptional profiles (Figure 5C,D). DEG analysis comparing astrocytes of 5w Aβ vs. ctrl hiNS(+)
466 highlighted significant upregulation of a number of genes associated with reactive astrocytes in
467 human AD. One of the most significantly upregulated genes was *APOE*, which is known to be the
468 largest genetic risk factor for sporadic AD and is expressed predominantly by astrocytes and
469 microglia in the human brain[36,70]. Surprisingly, our results show that Aβ induced upregulation of
470 *APOE* depends on the presence of hiMG. *APOE* is closely involved in amyloid clearance, and its
471 alleles ε2 and ε4 are extensively studied for their protective and deleterious roles, respectively[71].
472 The iPSC-line used in this study carries homozygous ε3 alleles not associated with any changes
473 in AD risk.

474 Cytokines produced by microglia are known to shape astrocyte activation states[72,73]. We found
475 that the addition of hiMG to hiNS increases the soluble level of a range of different cytokines in

476 the cell culture media (Figure 4G) and we found hiMG to be able to change the astrocytic
477 transcriptomic state under control conditions (Figure 1). We hypothesize that microglial cytokines
478 are the key driver in shaping astrocyte function in our neurosphere model system.

479 Our data indicates a previously unknown microglia-astrocyte crosstalk in AD and speculate that
480 hiMG cytokine production could be the trigger for *APOE* expression in astrocytes since a crosstalk
481 of cytokine and *APOE* expression has been reported in various tissues and model systems[74]. A
482 number of other genes of interest were also only upregulated in the presence of hiMG: 1) *LRP1*
483 is a receptor for APOE and has been associated with neuroprotection in animal models of AD[75,76],
484 2) *CLU* is an extracellular chaperone linked to neuroprotection via Aβ aggregation and clearance
485 by astrocytes[77,78], and 3) *VIM* was reported to be upregulated in AD although its role in pathology
486 remains elusive[79-81]. Significant gene ontology processes in 5w Aβ hiNS(+) astrocytes included
487 Aβ binding, phagocytosis and endocytosis, indicating that, in the presence of microglia, astrocytes
488 become reactive and could participate in Aβ clearance. Next, we analyzed astrocytes comparing
489 DEGs of hiNS(-) vs hiNS(+) after 3w/5w Aβ treatment separately to identify more microglia-
490 dependent astrocyte genes. Many DEGs were re-identified to the previous 5w Aβ hiNS(+) vs ctrl
491 hiNS(+) comparison such as *VIM*, *SPP1*, *APOE*, *LRP1* and *S100A11*, highlighting the importance
492 of hiMG in driving astrocyte gene expression (Figure 5I). Interestingly, *GFAP* was significantly
493 upregulated in hiNS(+) astrocytes compared to their hiNS(-) counterpart in both 3w and 5w Aβ
494 comparisons. Note that *GFAP* was not differentially expressed when comparing 5w Aβ hiNS(+) to
495 ctrl hiNS(+) astrocytes earlier, although our immunofluorescence analysis strongly indicates an
496 increase in GFAP immunoreactivity indicating astrocyte activation (Figure 4C). Our snRNA-seq
497 quantification of astrocyte numbers (Figure 5E) indicates that 5w Aβ hiNS(+) harbors the largest
498 population of astrocytes compared to all other groups. Therefore, the increased GFAP
499 immunoreactivity could be a result of either or both an increase in astrocyte numbers or increase
500 in *GFAP* expression. This highlights possible limitations of snRNA-seq, as it only captures mRNA
501 still inside the nuclei at the time of tissue harvest, not the full transcriptome[82]. Upregulation of
502 *GFAP* in AD-associated astrocytes is a well-known biomarker for AD[80,83,84] and is believed to be
503 associated with a neuroprotective reactive phenotype[85,86]. A recent study described a loss of
504 homeostatic gene expression in AD astrocytes, including downregulation of *NRXN1* and
505 *CADM2*[87]. Both genes were significantly downregulated in astrocytes of 3w/5w Aβ hiNS(+)
506 compared to hiNS(-), indicating hiMG dependence. Another gene of interest that was
507 downregulated is *SLC7A11*. Since its upregulation was recently associated with neurotoxic
508 functions of astrocytes[88], this further supports a neuroprotective astrocyte phenotype in the
509 presence of hiMG.

510 The presence of hiMG in 3w Aβ hiNS dramatically ameliorated Aβ induced oxidative stress (Figure
511 4D). Interestingly, we identified genes linked to oxidative stress response in astrocytes (*OXR1*,
512 *CCL2*, *CHL1)* were significantly upregulated with hiMG, indicating astrocytes could play a role in
513 reducing neuronal oxidative stress. *OXR1* increases oxidative stress resistance[88]. A recent study
514 found upregulation of *OXR1* following omaveloxolone treatment in a mouse model of AD linked
515 to markedly reduced AD pathology[89]. *OXR1* therefore could be an interesting target for future
516 studies.

517 We further found that hiMG in 5w Aβ hiMG(+) sub-cluster into three distinct populations including
518 one group resembling a unique transcriptional profile of damage associated microglia[35] which
519 includes the expression of *APOE* and *TREM2*, two genes extensively studied in AD research.

520 Overall, our snRNA-seq analysis indicates that astrocytes, in the presence of hiMG, and hiMG
521 themselves during our chronic Aβ model acquire neuroprotective reactive phenotypes matching
522 gene expression of human AD-glia. Our here presented model therefore offers unique
523 opportunities to study AD pathways involving neuron-glia-Aβ interaction to identify new
524 therapeutic targets for the treatment of AD.

525 **Acknowledgments**

526 We would like to thank Ken McArthur, the Aunie Foundation and the Copland family for their
527 generous donations to fund this project. We also thank the Alzheimer's Association and
528 Canadians For Leading Edge Alzheimer Research (CLEAR) for their support. For identifying the
529 *APOE* genotype of the used iPSC line we thank Dr. Mari DeMarco for assistance.

530 **Methods**

531 **Generation of human iPSCs and induction of NPCs**

532 The presented work on hiPSCs was approved by the University of British Columbia's Clinical
533 Research Ethics board. A single cell line was used, obtained from a healthy female individual
534 carrying the *APOE* alleles ε3/ε3. Peripheral blood was drawn and hiPSCs were generated from
535 erythroid progenitor cells. The cell line has been used and characterized by our laboratory in the
536 past[90,91].

537 hiPSCs were grown on Matrigel (BD Biosciences, Franklin Lakes, USA) coated 6-well plates in
538 mTeSR™ Plus (STEMCELL Technologies, Vancouver, Canada). Media was supplemented with
539 10 μM Y-27632 (EMD Millipore, Burlington, USA) for 24h after plating. Cells were fed every 2-3
540 days and used for both the induction of neural progenitor cells (NPCs) and microglial
541 differentiation. For storage, cells were frozen in media, supplemented with Y-27632 and 10%
542 DMSO (EMD Millipore) in liquid nitrogen (LN).

543 hiPSCs to NPC differentiation was achieved by a dual SMAD inhibition protocol as described
544 before[92]. In short, hiPSCs were plated in 6-well plates in Basal Neural Maintenance media
545 (BNMM) (Suppl. Table 1) supplemented with 10 μM SB-431542 (Tocris, Bristol, United Kingdom)
546 and 0.5 μM LDN-193189 (Tocris) for 7 days, followed by a 3-week differentiation in Neural Stem
547 Cell Media (see Supplementary Table 1) with media changes every 2-3 days. NPCs were then
548 expanded and passaged twice before freezing them down in LN (BNMM supplemented with Y-
549 27632 and 10% DMSO) at P2.

550 **Neurosphere generation**

551 To generate human iPSC-derived neurospheres (hiNS), P2 NPCs were thawed and plated in
552 Matrigel-coated 6-well plates using Neurosphere Expansion Media (NEX) (Suppl. Table 1)
553 supplemented with 10 μM Y-27632 for 24h. Cells were fed every 2-3 days and allowed to recover
554 for at least 5 days until the cell density was sufficient to start hiNS generation. To start hiNS
555 formation, NPCs were lifted using Accutase (STEMCELL Technologies) and plated in single wells
556 of AggreWell™800 plates at a density of 1.2 * $10^6$ NPCs per well in NEX supplemented with 10
557 μM Y-27632 for 24h and centrifuged for 2 min at 100g. hiNS were fed daily by careful partial media
558 changes until day 7 (days in vitro, DIV 7). At DIV7 hiNS were dislodged using wide bore tips and
559 37 μm reversible strainers (STEMCELL Technologies) and transferred to standard 10 cm cell
560 culture petri dishes in Neurosphere Differentiation Media (NDM) (Suppl. Table 1) and immediately

561 placed on an orbital shaker (Celltron, Infors HT, Bottmingen, Switzerland) in the cell culture
562 incubator at 65 rpm. hiNS were fed every 2-3 days by full media change and switched to
563 Neurosphere Maintenance Media (NMM) (Suppl. Table 1) on DIV 28. hiNS were kept in the petri
564 dishes until DIV 39-41 when they were transferred to Matrigel coated (1% overnight) single wells
565 of 48-well plates for future experiments either on regular cell culture plates, 8 mm coverslips or
566 glass bottom live imaging plates (MatTek, Ashland, USA). For precise positioning on glass
567 surfaces a tissue dissection microscope (Zeiss Stereo Discovery V8) was used inside a biosafety
568 cabinet. Plated hiNS readily attach to surfaces allowing for easy confocal live imaging. To induce
569 the expression of genetically encoded fluorescent proteins, hiNS were transduced with 0.5-0.75
570 μL of custom AAVs (AAV2/PHP.eB) on the day of plating. Promoters used were *gfaABC1D* (for
571 EGFP) and *hSyn* (for mCherry, roGFP1, GCaMP6f and iGluSnFr) and all AAVs titers ranged from
572 1-2 * $10^{13}$ gene copies per mL. After plating and transduction, hiNS media was partially changed
573 every 2-3 days.

574 **Differentiation of human iPSC-derived microglia**

575 Human iPSC-derived microglia (hiMG) were differentiated based on a protocol by the Cowley lab
576 with minor adjustments[90] as follows. hiPSCs were collected from 6-well plates using Accutase and
577 1.5 * $10^6$ cells were added to a single well of an AggreWell™800 plate in Embryoid Body Media a
578 (Suppl. Table 1) and centrifuged at 100g for 2 min. Media was changed daily for 4 days. On day
579 5, EBs were collected using a wide bore tip and a 37 μm reversible strainer and resuspended in
580 10 mL Hematopoietic Differentiation Media (HDM) (Suppl. Table 1) in a standard T75 Cell Culture
581 flask. The flask was kept in the incubator for 7 days without feeding or moving for EBs to attach
582 to the surface. Afterwards, EBs were fed with 5 mL of HDM twice a week. As early as day 35,
583 accumulating macrophage precursors were harvested for subsequent microglia differentiation.
584 Collected HDM enriched with macrophage precursors was centrifuged at 400g for 5 min and cells
585 were resuspended in Microglial Differentiation Media (MDM) (Suppl. Table 1) and plated in 6-well
586 glass bottom plates at densities of 0.75-1 * $10^6$ cells/$cm^2$. Partial media changes were conducted
587 every 2-3 days with MDM and hiMG were allowed to differentiate for 10-14 days.

588 **Microglia transfer into neurospheres**

589 Mature hiMG after 10-14 days of differentiation were collected using TrypLE Express (Thermo
590 Scientific, Waltham, USA) and resuspended in NMM supplemented with 100 ng/mL IL-34
591 (BioLegend, San Diego, USA)) and 25 ng/mL TGFβ1(PeproTech, Cranbury, USA) and added to
592 well-attached hiNS in 48-well plates at a density of 35,000 cells/well between DIV 49-60. hiNS(+)
593 were fed with partial media changes every 2-3 days with NMM supplemented with IL-34/TGFβ1.

594 **ELISA**

595 For multiplex ELISA assays of hiNS media, the supernatant of 6 individual hiNS (across all
596 treatment groups) was pooled together and frozen at -80°C. Before analysis, samples were
597 thawed on ice and concentrated using Amicon Ultra 3kDa centrifugal filters (EMD Millipore) by
598 centrifuging 500 μL at 14,000g for 15 min. This step was repeated twice until all media was
599 concentrated. Concentrated media was then collected after flipping the filter and centrifuging
600 again at 1000 g for 2 minutes. The resulting total volume for each pooled sample of concentrated
601 media was ~80 μL. For soluble Aβ quantification the V-PLEX Aβ Peptide Panel 1 (4G8) (Meso
602 Scale Diagnostics, Rockville, USA) was used for electro chemiluminescent detection
603 of Aβ38, Aβ40, and Aβ42 in concentrated supernatant. Samples were diluted 1/5,000 in Diluent

604 35 (provided in the kit). All samples and calibrators were run in duplicate following manufacturers'
605 instructions. To quantify cytokine expression in hiNS media, the same samples were used for the
606 V-PLEX Cytokine Panel 1 Human Kit (Meso Scale Diagnostics) for the quantification of ten
607 cytokines: GM-CSF, IL-1α, IL-5, IL-7, IL-12/IL-23p40, IL-15, IL-16, IL-17A, TNF-β, and VEGF-A.
608 All concentrated samples were diluted 15x and all samples/calibrators were run in duplicate
609 following the manufacturer's instructions. MESO QuickPlex SQ 120MM was used for plate reading
610 and protein concentrations were determined using the Discovery WorkBench Software provided
611 by Meso Scale. For cytokine quantification, concentrated supernatant protein concentration was
612 detected via BCA for normalization of cytokines between samples.

613 **Oligomeric Aβ preparation**

614 Synthetic lyophilised Aβ1-42 (ERI Amyloid Laboratory, New Haven, USA) was mixed thoroughly
615 and dissolved in 40 µL of DMSO for 20 minutes at room temperature (RT) at a concentration of
616 ~2 mM. The mixture was then separated into two 20 µL aliquots and 1 mL of F12 (Thermo
617 Scientific) media was added to each aliquot. The dissolved Aβ was incubated at RT for 24 hours
618 to induce oligomerization. Next, 500 µL of the oligomeric Aβ1-42 (Aβ) was centrifuged at 14,000
619 g for 15 minutes using Amicon Ultra 3kDa centrifugal filters. This was repeated 3 times to
620 concentrate the Aβ. The Aβ was then washed twice with 500 µL of PBS and centrifuged at 14,000
621 g for 15 minutes. The filters were then flipped onto collection tubes and centrifuged at 1000 g for
622 2 minutes to collect the Aβ. The final Aβ was stored at –80°C. To determine the final Aβ
623 concentration we used a multiplex Aβ (6E10) ELISA panel (see above) on four different batches
624 of Aβ. The final stock concentration of Aβ was 0.24 ± 3.4 mg/mL.

625 To conjugate Aβ with pHrodo red/green (Thermo Scientific), 2 µL were added into each 1 mL of
626 the F12/Aβ mix prior to centrifugation and incubated at 4°C in the dark for 3 hours. Centrifugation
627 steps were continued afterwards as described above with one additional PBS washing step and
628 the conjugated pHrodo-Aβ was stored in the dark at -80°C.

629 **Chronic Aβ treatment paradigm**

630 To model chronic amyloidosis in our 3D neurosphere cultures, we supplemented NMD/NMM with
631 Aβ in a 1:1000 dilution resulting in a final Aβ concentration in the media to be 0.24 μg/mL. Aβ was
632 added during partial media changes (150 μL from a total of 400 μL per well) calculated for the
633 total volume of the wells resulting in a gradual increase of aggregated Aβ over time. The duration
634 of Aβ treatment was either 3 or 5 weeks. For the control groups (ctrl hiNS(-/+)), media was
635 supplemented with 3.6 μg/mL scrambled Aβ42-1 for a total of 3 weeks.

636 **Confocal microscopy of neurospheres**

637 For live neurosphere imaging, hiNS were plated and transduced with AAVs in 48-well glass bottom
638 plates as described above. hiNS were imaged 7-10 days post transfection using a confocal
639 microscope equipped with a live imaging incubator system (LSM 880, Zeiss, Oberkochen,
640 Germany). For *hSyn*-GCaMP6f and *hSyn*-iGluSnFr, 3-5 min time series were recorded of green
641 emission excited using a 488 nm argon laser. hiNS display synchronized wave-like neuronal
642 activity leading to rises in neuronal calcium levels (quantifying GCaMP6f) or a rise in extracellular
643 glutamate concentrations (quantifying iGluSnFr) (Figure 1). AQuA[93] was used for calcium wave
644 quantification as follows. For each hiNS, calcium activity was recorded at one z-plane for 300
645 frames at a frame rate of 0.931 seconds per frame, and the resolution was 0.692 μm per pixel.

646 Prior to analysis, the resolution was downsized to 1.384 μm/pixel in FIJI to allow for smoother
647 processing. In AQuA, an ROI was drawn around each neurosphere. For event detection, AQuA
648 uses the parameters intensity threshold, smoothing, and minimum pixel size, which were adjusted
649 so that signals that spanned the entire neurosphere were counted as a single event, and other
650 background single cell activity was classified as noise and ignored.

651 To quantify neuronal redox states in hiNS we employed roGFP1[19], a genetically encoded redox
652 indicator we have used in the past[20]. roGFP is a ratiometric indicator in which upon oxidation, the
653 excitation spectrum of roGFP shifts to lower wavelengths (~400 nm) while fully reduced roGFP
654 has a maximum excitation peak at ~490 nm. The green fluorescence of roGFP on the other hand
655 is not affected by its redox states. Therefore, roGFP1 was imaged on our live imaging confocal
656 microscope alternately with either a 405 nm laser (maximum excitation for oxidized roGFP1) and
657 a 488 nm laser (maximum excitation for reduced roGFP1) to quantify neuronal redox states
658 across experimental conditions. Laser settings were kept constant and green emission for both
659 excitation wavelengths were captured and averaged across a 30 μm z-stack. The '*roGFP1 ratio'*
660 (Figure 1) was defined as green emission acquired exciting at 405 nm and divided by green
661 emission acquired exciting at 488 nm. For one data set (Figure 3D) hiNS expressing roGFP1
662 were fixed in 4% PFA substituted with 20 mM N-Ethylmaleimide to preserve the redox state of
663 roGFP1 allowing post-fixation redox imaging[20].

664 **Human formalin-fixed paraffin-embedded (FFPE) Magnified Analysis of Proteome (MAP)**
665 **tissue clearing and expansion**

666 The FFPE MAP procedure was adapted from the original MAP procedure[94] with slight
667 modifications[37]. Three FFPE brain sections with 4 μm thickness were used, two familial AD
668 patients and one sporadic AD patient.

669 *Deparaffinization and rehydration:*

670 High precision #1.5 coverslips were cut and glued directly on the original slides to which the
671 sections were attached on each side of the sections. These served as spacers for the gel
672 embedding (see below). Then sections were deparaffinized and rehydrated by washing them
673 with xylene three times for 5 min each and then two times for 5 min each in the following
674 solutions: 100% ethanol 95% ethanol, 70% ethanol, and 50% ethanol. Finally, the samples were
675 rinsed two times with deionized water for 5 min each. From this step onward, samples were
676 protected from light.

677 *Post-fixation:*

678 Sections were kept in fixative solution (4% PFA in PBS) for 2 h at 37°C then washed three times
679 in washing solution (PBS with 0.02% of NaN3) from 30 min each at 37°C with gentle shaking.

680 *AA-integration:*

681 Sections were incubated in low-AA solution (4% acrylamide (Sigma Aldrich, A3553), 4% PFA in
682 PBS) at 4°C with agitation overnight, followed by a 2 h incubation at 37°C with gentle shaking.

683 *Inactivation:*

684 Brain sections were washed with washing solution three times at 37°C for 30 min each.
685 Sections were then incubated in Inactivation solution (1% acetamide (Sigma Aldrich, A0500),

686 1% glycine (Sigma Aldrich, G7126), 0.02% NaN3 (Sigma Aldrich, S2002) with the pH titrated to
687 9.0 with NaOH) at 37°C for 3 h with gentle shaking.

688 *Monomer incubation:*

689 Brain sections were washed with washing solution three times at 37°C for 30 min each. MAP
690 solution was made by freshly adding V-50 initiator (Sigma Aldrich; 440914) to a solution of 30%
691 acrylamide, 0.1% bisacrylamide (Sigma Aldrich, M7279), and 10% sodium acrylate (Sigma
692 Aldrich, 408220) in PBS; the brain sections were incubated in MAP solution overnight at 4°C
693 with gentle shaking.

694 *Mounting and gel embedding*:

695 The gelation was done directly on the original slides to which the sections were attached. 100
696 µL of MAP solution with freshly added V-50 initiator was placed directly on each section and
697 topped with a coverslip to form gelation chambers. Gelation chambers were placed in a humid
698 gelation box which was sealed, and the air purged with nitrogen gas. The gelation box was put
699 in the oven at 45°C for 2 h 30 min, following which the hybrid gel–tissue was removed and
700 excess gel around the tissue cut away.

701 *Denaturation, clearing, and expansion:*

702 The tissue–gel hybrid sections still attached to the slides were immersed in denaturation
703 solution (in mM, 200 SDS, 200 NaCl, 50 Tris, pH 9) and incubated at 65°C for 3 days with gentle
704 shaking using an EasyClear device (LifeCanvas Technologies). The FFPE-MAP tissue–gel
705 hybrids generally floated free of the slides after denaturation. Sections were washed 4 times for
706 1 h each with 0.001× PBS and gentle shaking and then incubated in 0.001× PBS at RT
707 overnight with gentle shaking. To prepare the sections for immunostaining, the 0.001× PBS was
708 replaced with PBST (0.1% Triton X-100 in PBS) for 1 h before staining. The side that had been
709 facing the original slide, thus which had the tissue at the surface, was mounted next to the
710 coverslip for imaging.

711 **Immunofluorescence**

712 For immunofluorescence staining, hiNS were plated on 8 mm glass coverslips and fixed in 4%
713 paraformaldehyde for 1h. Fixed hiNS were washed and kept in PBS at 4°C before staining.
714 Immunofluorescence stainings were conducted as described before[20]. hiNS were either stained
715 in full or sliced with a vibratome into 80 µm thin sections (VT1200, Leica, Nussloch, Germany)
716 before immunostainings. In brief, hiNS (full or slices) were blocked with 10% normal donkey
717 serum (NDS) (Jackson ImmunoResearch, West Grove, USA) in 0.1M PBS containing 2% Triton
718 X-100 and 20% DMSO for 1h. Afterwards, samples were washed once with PBS before incubating
719 in primary antibody solution containing 0.1M PBS, 2.5% NDS, 2%Triton X-100 and 20% DMSO.
720 Primary antibodies used were Aβ (6E10), 1:500 (BioLegend, San Diego, USA); Aβ (4G8), 1:500
721 (BioLegend); Aβ (mOC87), 1:500 (abcam, Cambridge, United Kingdom); GFAP, 1:1500 (Thermo
722 Scientific); MAP2, 1:1500 (abcam); IBA1, 1:500 (FUJIFILM Wako Chemicals, Richmond, USA);
723 Cleaved Caspase-3, 1:500 (Cell Signaling Technologies, Danvers, USA). Afterwards, samples
724 were thoroughly washed with PBS 3-4 times before incubating in secondary antibody solution
725 containing 0.1M PBS, 2.5% NDS, 2%Triton X-100 and 20% DMSO and secondary antibodies
726 targeted against the host species of primary antibodies conjugated with either Alexa Fluor 405,
727 488, 568 or 647 (Thermo Scientific) and incubated for 1h. For quantification of apoptosis, TUNEL

728 (Click-iT™ Plus, Invitrogen) was used following the manufacturer guidelines after
729 immunostainings were performed. After 3-4 washing steps in PBS, stained hiNS were imaged on
730 the LSM 980 confocal microscope (Zeiss). Quantification of fluorescence was performed using
731 FIJI (ImageJ 1.53t). The immunostaining protocol for FFPE MAP human sections was performed
732 the same way except for using a 0.1% Triton-X-100 PBS solution for blocking and staining buffers
733 instead of the 2% Triton-X-100/20% DMSO mix.

734 **Western Blot**

735 Western blot analysis was performed on differentiating hiMG harvested at different time points.
736 Cell lysates were prepared using RIPA lysis buffer supplemented with phosphatase and protease
737 inhibitor cocktail (Roche, Basel, Switzerland), followed by centrifugation at 13,000g for 10 minutes
738 at 4°C. The resulting supernatant was diluted with 4x Laemmli sample buffer and boiled for 5
739 minutes before loading onto Mini-Protean TGX gels (Bio-Rad, Hercules, USA). Subsequently,
740 SDS-PAGE was conducted, and the separated proteins were transferred onto PVDF membranes
741 using a Trans-Blot Turbo semi-dry transfer system (Bio-Rad). Membranes were blocked using 3%
742 BSA in TBS with 0.1% Tween20 (TBST), followed by overnight incubation at 4°C in TBST with
743 primary antibodies against IBA1 (GTX635400, 1:500, GeneTex, Irvine, USA,) or GAPDH
744 (PA1988, Thermo Scientific, 1:1000). After washing, membranes were probed with HRP-
745 conjugated secondary antibodies (Jackson ImmunoResearch) for 2 hours at room temperature.
746 Protein bands were visualized using Bio-Rad Clarity Western ECL substrate and imaged with a
747 ChemiDoc MP imaging system. Protein band size and intensity were quantified using ImageJ
748 software.

749 **Electrophysiology and 2-photon imaging**

750 Patch-clamp recordings on microglial cells were performed on hiNS(+) either ctrl or Aβ (3w/5w)
751 treated after plating them on coverslips, which allowed moving them to a 2-photon microscope for
752 patch-clamp and image recordings (Zeiss 510Meta microscope with a Ti:Sapphire Chameleon
753 laser). hiMG were stained with 2 μL tomato-lectin-488 (for patch-clamp) or 594 (for process
754 motility quantification) (Thermo Scientific) per well for 30 min to allow for the identification of
755 microglia in neurospheres using the 2-photon microscope. hiNS were supplied with a continuous
756 perfusion of carbogen (95% $O_2$/ 5% $CO_2$) infused BrainPhys Imaging Optimized media
757 (STEMCELL Technologies) and the following intracellular solution was used for microglial patch-
758 clamp recordings, as described before (in mM)[28,29]: KCl,130; $MgCl_2$,2;$CaCl_2$, 0.5; Na-ATP, 2;
759 EGTA, 5; HEPES, 10 and sulforhodamine 101, 0.01 (Sigma Aldrich) at an osmolarity of ~370
760 mOsm and a pH of 7.3. Borosilicate patch pipettes were pulled with a final pipette resistance of
761 3-5 MΩ. hiMG were targeted using the lectin fluorescence and clamped at -40 mV after reaching
762 whole-cell configuration. A series of de- and hyperpolarizing voltage steps were applied ranging
763 from -150 to + 60 mV with 10 mV increments and patched hiMG with abnormally small
764 capacitances (<10 pF) or a series resistance of >65 MΩ were discarded. To test if hiMG perform
765 surveillance functions and respond to tissue damage, ctrl hiNS(+) (N=3) were stained with lectin-
766 594 and z-stack (27 μm thick) time series were acquired using our 2-photon microscope at 850
767 nm. After recording a baseline to monitor process movement, a laser lesion was burned into the
768 centre of the neurosphere by tuning the laser to 800 nm at 100% power for 15 seconds. hiMG
769 process movement towards the lesion was then imaged again using 850 nm excitation
770 wavelengths in a z-stack time series recording.

771 **Single nuclei RNA sequencing**

Single nucleus capture was performed at the Princess Margaret Genomics Centre (Toronto, ON) using the relevant Genomics Chromium system protocol. Libraries were sequenced on the Illumina NovaseqX Plus instrument. FASTQ reads were aligned to the wild-type human genome (hg38) using the relevant 10x Genomics Cell Ranger software. Output data was analyzed using a previously described computational pipeline[21-25]. In brief, cells with low UMI counts, red blood cells, cells with high mitochondrial DNA content, and putative doublets were removed. Genes detected in fewer than three cells were removed and cell transcriptomes were normalized using the scran R package to account for read depth and library size[22]. The Seurat package (v4.2.0)[21] was then used to process the normalized expression matrices. Following this, principal component analysis (PCA) was performed using the top 2000 highly variable genes. Next, the top principal components were used to project the dataset into two-dimensional space as Uniform Manifold Approximation and Projection (UMAP) embeddings using the RunUMAP function in Seurat. Afterwards, the top principal components were also used to iteratively carry out SNN-Cliq-inspired clustering using the FindClusters function in Seurat at resolutions ranging from 0.2 to 2.4. Each dataset was analyzed by choosing the most conservative resolution; resolution was only increased to interrogate cell heterogeneity or if two cell populations of known identity, based on the expression of canonical markers, were not separating into distinct clusters as expected. To merge or subset datasets, barcodes corresponding to the cells or cell types of interest were used to extract relevant gene expression information from filtered gene expression matrices. For the merging of datasets, the gene expression information from each respective dataset was then combined. The cells were then once again run through the pipeline as described above.

For the hiNS(-/+) merged dataset (as in Figure 1A), clusters were assigned at a resolution of 0.4 (16 clusters identified with at least 107 DEGs between most similar clusters, FDR < 0.01). To generate the subsetted astrocyte dataset (as in Figure 1D), cells from cluster 0 (res. 0.4) were extracted and run through the pipeline. Clusters were assigned at a resolution of 0.2 (4 clusters identified with at least 112 DEGs between most similar clusters, FDR <0.01). For the hiNS(-/+) in control, 3w and 5w Aβ merged dataset (as in Figure 5A), clusters were assigned at a resolution of 0.4 (16 clusters identified with at least 204 DEGs between most similar clusters, FDR < 0.01). To generate the subsetted astrocyte dataset (as in Figure 5C), cells from cluster 0 (res 0.4) were extracted and run through the pipeline. Clusters were assigned at a resolution of 0.2 (4 clusters identified with at least 112 DEGs between most similar clusters, FDR <0.01).

**DEG statistical analysis**

DEG analysis of snRNA-seq data was performed using the FindMarkers function in Seurat. Expression levels were tested using a Wilcoxon Rank Sum Test. A Bonferroni-adjusted p-value smaller than 0.05 (padj < 0.05), coupled with an average fold-change of greater than 1.4 (FC > 1.4), was considered statistically significant.

**Gene ontology analysis**

g:Profiler (version e109_eg56_p17_1d3191d, https://biit.cs.ut.ee/gprofiler/)[95] was used to determine which gene ontology (GO) terms were significantly differentially overrepresented in cell populations following gene expression (fold-change > 1.4, adjusted p- value < 0.05) comparisons. If multiple Ensembl IDs were detected for a particular gene, the ID with the most GO annotations was used. In cases with multiple IDs with the same number of GO annotations, the first ID was used. Some genes were excluded from analysis if Ensembl IDs could not be

found. The g:SCS multiple testing correction algorithm was used for p-value correction with a significance threshold of 0.05.

**Pearson and single-cell correlation analyses**

Pearson correlation analysis (Figure 1H) was performed by averaging the expression of a given transcript within each cluster/cell type of interest and correlating the expression values between clusters/cell types using the cor.test function in R.

**Statistical analysis**

For the comparison of calcium wave frequencies (quantified by GCaMP6f imaging), paired student-t-tests were used for pharmacological experiments and comparing two different time points. Unpaired student t-tests were used when comparing baseline calcium wave frequencies, Aβ phagocytosis, immunoreactivity and nuclei density of control hiNS vs. Aβ treated hiNS. For comparing microglial densities and GFAP immunoreactivity between control, 3w Aβ and 5w Aβ hiNS(+) ordinary one-way ANOVA followed by Holm-Sidak post-hoc tests were used. Logarithmic transformation was done on all data sets comparing control, 3w Aβ and 5w Aβ hiNS with or without hiMG prior to using two-way ANOVAs, testing for the effect of hiMG, followed by Holm-Sidak post-hoc tests. Statistical significance was indicated as follows: * $p < 0.05$; ** $p < 0.01$; *** $p < 0.001$; **** $p < 0.0001$.

833 **Figures legends**

834 **Figure 1:** Human iPSC-derived mixed cell type neurospheres (hiNS) are comprised of neurons
835 and glia. **A**: Schematic of hiNS generation and infiltration of human iPSC-derived microglia (hiMG)
836 to form mature hiNS. hiNS after hiMG infiltration are defined as hiNS(+) while labelled hiNS(-) in
837 the absence of hiMG. **B**: Redox imaging of hiNS(-) following transduction with AAV.php.eb.hSyn-
838 roGFP1. Resting redox states of hiNS(-) (N=6) were only slightly higher than that of fully reduced
839 DTT (5mM) -treated hiNS (N=5) indicating healthy neurons throughout the 3D tissue. Full
840 oxidation by diamide (2 mM) (N=4) indicates maximum roGFP ratios **C**: Single nuclei RNA
841 sequencing (snRNA-seq) on hiNS(+/-). Overview of identified cell clusters and cell type
842 identification in a merged data set of both groups **D**: Expression pattern of genes across cell
843 populations for neuronal, astrocytic and microglia/macrophage displaying example marker genes.
844 **E**: Datasets of origin confirming the presence of microglia/macrophage (marked in green) is
845 exclusive to hiNS(+) and that astrocyte gene expression (marked in red) appears shifted by the
846 presence of hiMG. **F**: UMAP of isolated astrocyte populations from both data sets reveals 3
847 distinct sub-clusters with clusters 0b and 0c predominantly in hiNS(+) astrocytes and cluster 0a
848 preferentially in hiNS(-) astrocytes. **G**: Analysis of the dataset of origin illustrating the shift in
849 astrocyte gene expression in the presence of microglia. **H**: Pearson correlation (r = 0.978)
850 confirms the close similarities between the two astrocyte populations. **I**: Differential gene
851 expression (DEGs) pattern of a selection of DEGs shown in heatmaps. **J**: Gene ontology analysis
852 of astrocyte clusters with and without hiMG.

853 **Figure 2:** Neurons and glia are highly functional in hiNS mimicking early brain physiology. **A**:
854 Immunofluorescence of MAP2, GFAP and IBA1 in a mature neurosphere at day in vitro (DIV) 60.
855 **B**: Functional intracellular calcium (AAV.php.eb.-*hSyn*-GCaMP6f) and extracellular glutamate
856 (AAV2/9-*hSyn*-iGluSnFr) imaging shows highly synchronized calcium and glutamate activity in
857 hiNS(-). **C**: Spontaneous neuronal calcium activity traverses through hiNS in a wave-like manner.
858 **D**: Pharmacological block of calcium waves by TTX (1 μM) (N=6), AP5 (100 μM)/CNQX (20 μM)
859 (N=6) and GABA (300 μM) (N=6). Application of picrotoxin (100 μM) (N=4) resulted in a significant
860 increase in calcium wave frequencies. **E**: Infiltration of hiMG in hiNS(+) results in a significant
861 reduction in calcium wave frequencies with longer wave durations (hiNS(-): N=10; hiNS(+): N=12).
862 **F**: Long-term confocal imaging of transduced hiNS(+) (N=4) with AAV.php.eb-hSyn-mCherry (red)
863 and AAV.php.eb-gfaABC1D-EGFP (green) and tomato lectin DyLight 649 stained hiMG. hiMG
864 infiltration into the tissue was quantified within the first 24h post-transfer (see yellow arrows and
865 areas). **G**: hiMG within hiNS display surveillance behaviour with rapidly moving processes and a
866 more stationary soma. Tissue damage induced by a laser lesion leads to rapid process outgrowth
867 of microglia towards the lesion. **H**: Electrophysiological properties of hiMG 7-10 days post
868 infiltration (N=9).

869 **Figure 3:** Chronic Aβ stimulation in hiNS(-) triggers a sequence of neurotoxic events and
870 phenotypes in the absence of hiMG. **A**: hiNS(-) cell culture media was supplemented with ~0.24
871 μg/mL oligomeric Aβ1–42 for up to 35 days. **B**: Treatment results in the formation of plaque-like
872 Aβ aggregates in hiNS(-) which can be stained with different Aβ antibodies (here 6E10 and
873 mOC87). **C**: Immunostaining for neurons (MAP2) and astrocytes/NPCs (GFAP) after 35 days of
874 Aβ exposure reveals dystrophic appearing neuronal and astrocytic processes (see white arrows)
875 **D**: roGFP1 based redox imaging in neurospheres reveals significant oxidation indicating oxidative
876 stress in neurons following chronic Aβ treatment (N=4 each). **E**: Calcium wave frequencies
877 (quantified by GCaMP6f live imaging) gradually decline with Aβ treatment resulting in

878 dysfunctional neuronal activity (N=4 each). **F**: Immunostaining for cleaved Caspase-3 (c-Cas-3)
879 indicates apoptosis in hiNS(-) after chronic Aβ exposure. Quantification of DAPI positive nuclei in
880 hiNS(-) suggests neuronal death as the ultimate fate following 35 days of chronic Aβ treatment.
881 **G**: Co-staining for c-Cas-3/MAP2 indicates neurons undergoing apoptosis and loss of nuclei
882 density (N=4 each). **H**: Apoptosis after 35 days of Aβ exposure was further confirmed by a
883 significant increase in TUNEL fluorescence (control: N=4; Aβ: N=5).

884 **Figure 4:** Timing-dependent neuroprotection by hiMG in hiNS(+) during two different chronic Aβ
885 treatment protocols. **A**: Schematic illustrating 3-weeks (3w Aβ hiNS(+)) and 5-weeks (5w Aβ
886 hiNS(+)) long chronic Aβ protocols. In each, hiMG were transferred 10 days before the end of
887 both protocols. **B**: Quantification of hiNS areas covered by Aβ (stained for 4G8) reveals less Aβ
888 burden after 3w than 5w with a significant reduction in Aβ levels in 3w Aβ hiNS(+) compared to
889 3w Aβ hiNS(-) (N=6 each). At 5w soluble Aβ was significantly reduced in hiNS(+) supernatant at
890 DIV 60 measured using ELISA (4G8) (N=3; pooled supernatant from six individual hiNS each). **C**:
891 Immunofluorescence staining for MAP2, GFAP and IBA1 reveals a larger hiMG population in 5w
892 Aβ hiNS(+) compared to 3w Aβ hiNS(+) or controls (ctrl hiNS(+)) as well as an increase in GFAP
893 immunoreactivity in 3w/5w Aβ hiNS(+) (N=6 each). **D**: Redox imaging using roGFP1 indicates
894 mild oxidative stress in 3w Aβ hiNS(-) with a full rescue in 3w Aβ hiNS(+). Severe oxidative stress
895 in 5w Aβ hiNS(-) was not ameliorated by hiMG (N=6 each). **E**: Functional recovery in calcium
896 wave activity by hiMG in 3w Aβ hiNS(+) quantified using GCaMP6f. Calcium waves in 5w Aβ hiNS
897 were completely absent and hiMG did not result in a functional recovery (ctrl hiNS(-): N=10; ctrl
898 hiNS(+): N=12; 3w/5w Aβ hiNS(-/+): N=6 each). **F**: At both time points, hiMG resulted in a
899 reduction in c-Cas-3 immunoreactivity and ameliorated cell death (ctrl hiNS(-): N=9; ctrl hiNS(+):
900 N=11; 3w Aβ hiNS(-/+): N=10 each; 5w Aβ hiNS(-): N=8; 5w Aβ hiNS(+): N=11). **G**: Cytokine levels
901 in hiNS concentrated supernatant of all experimental conditions measured via multiplex ELISA
902 (N=3; pooled supernatant from six individual hiNS each). In all hiNS(-) samples, cytokine levels
903 were mostly undetectable or low. Cytokine production increases in hiNS(+) in ctrl and Aβ treated
904 hiNS with IL-6 and IL-12 levels significantly increased from ctrl hiNS(+) to 5w Aβ hiNS(+).

905 **Figure 5:** snRNA-seq on hiNS(-/+) in ctrl, 3w and 5w Aβ conditions reveals a hiMG-dependent
906 astrocyte AD-like transcriptional profile in 3w/5w Aβ hiNS(+). **A**: Merged UMAP of all 6
907 experimental groups displaying cell clusters and cell type identification. **B**: Split merged UMAPs
908 without hiMG (left) and with hiMG (right). Note the lack of a microglial population in hiNS(-),
909 reduced neuronal populations in the absence of microglia indicating severe cell loss after 5w Aβ
910 treatment. **C**: Isolated astrocyte population in a merged UMAP displaying four distinct clusters. **D**:
911 Data set of origin for all 6 conditions illustrating significant shifts of astrocyte gene expression
912 depending on Aβ treatment and hiMG presence. Dashed lines mark the rough outline of the
913 predominantly 3w/5w Aβ hiNS(+) astrocyte populations. **E**: Number of astrocytes sorted per sub-
914 cluster (top panel) and sorted by condition (bottom panel). Note that astrocyte numbers varied
915 between conditions with 5w Aβ hiNS(+) marking the largest astrocyte population. **F**: Differential
916 gene expression pattern of a selection of DEGs in 5w Aβ hiNS(+) astrocytes shown in heatmaps,
917 compared to ctrl hiNS(+). Note that upregulation of genes with Aβ treatment required the presence
918 of hiMG, including *APOE*. **G**: Overlay examples of AD-associated gene expression in astrocytes
919 in 5w Aβ hiNS(+) astrocytes. **H**: Gene ontology analysis of ctrl hiNS(+) and 5w Aβ hiNS(+)
920 astrocyte groups highlight distinct hiMG-dependent phenotypical differences in Aβ treated
921 astrocytes. **I**: Direct comparison of DEGs depending on hiMG in 3w (left) and 5w (right) Aβ treated

922 hiNS shown in volcano plots (compared in pairs). Genes of interest are labelled. Note that many
923 AD-associated genes, such as *GFAP*, *VIM* and *APOE*, are only upregulated if hiMG were present
924 during Aβ treatment.

925 **Figure 6**: hiMG after chronic Aβ treatment are a heterogeneous cell population of microglia and
926 macrophage-like cells mimicking AD. **A**: The subset of hiMG generated from cell cluster 13 (Figure
927 5A) from the 5w Aβ hiNS(+) data set reveals three distinct sub-clusters (13a-c). **B**: Overlay
928 examples are shown for each cluster of hiMG. **C**: Gene ontology analysis suggests different
929 biological properties of each cluster. **D**: Volcano plots of DEGs with highlighted genes of interest,
930 including *APOE* in cluster 1 of DAM-like microglia.

931 **Figure 7:** APOE expression in hiNS and human AD. **A**: APOE immunofluorescence in hiNS slices
932 reveals large quantities of extracellular APOE in 5w Aβ hiNS(+). **B**: Quantification of APOE
933 immunofluorescence (ctrl hiNS(-/+): N=4 each; 3w Aβ hiNS(-/+): N=5 each; 5w Aβ hiNS(-/+): N=5
934 each). **C**: Intracellular APOE identified in hiMG (stained for IBA1, cell labelled 'mg') and astrocytes
935 in 5w Aβ hiNS(+). **D**: Co-staining of APOE with 4G8 indicates that extracellular APOE is in close
936 proximity to Aβ aggregates close to the surface of hiNS (N=3 each). **E**: Immunofluorescence
937 staining in cleared and expanded human AD post-mortem brain sections confirms the close
938 proximity of APOE with Aβ deposits and intracellular APOE in astrocytes in AD (N=3, 1 sporadic
939 AD, 2 familial AD).

940 **Figure S1:** hiMG differentiation timeline shows a gradual increase in IBA1 expression. **A**: hiMG
941 were plated on coverslips and fixed at different time points during differentiation (8 to 21 days)
942 (N=3 coverslips each time point). Immunofluorescence for IBA1 (magenta) is detectable at all
943 time points. Co-staining with tomato lectin-488 confirms that lectin can be used to label hiMG *in*
944 *vitro*. **B**: Western blot for IBA1 confirms stable expression in hiMG up to at least day 21 (N=3
945 each). **C**: Stimulation of hiMG with LPS for 24h results in significant TNFα and IL1β release
946 confirming their capacity to react to proinflammatory stimuli (N=3 each).

947 **Figure S2:** Over-night live confocal imaging of hSyn-roGFP1 expressing hiNS(-) during chronic
948 Aβ treatment. Recordings of 18-22h duration were conducted between DIV 87-104 with chronic
949 Aβ treatment ranging from 7 to 23 days (N=5 over-night recordings each). **A**: Example section of
950 an Aβ treated hiNS displaying multiple neurons oxidizing during the recording time period (see
951 arrows). **B**: The total number of oxidizing cells per hour was quantified for both Aβ treated as well
952 as control hiNS. In Aβ treated spheres 0.29 ± 0.02 cells oxidized per hour compared to 0.07 ±
953 0.01 under control conditions (student's t-test, **** $p<0.0001$).

954 **Figure S3:** Example transmitted light images of control and Aβ treated hiNS with and without
955 hiMG. hiMG attach to the surface surrounding hiNS Note that 5w Aβ hiNS (+/-) display a darker
956 contrast and appear to detach from the surface (see red arrows).

957 **Figure S4:** hiMG are effective in phagocytosing Aβ and facilitate APOE expression. **A**: Co-
958 localization of Aβ in IBA1 or lectin-stained hiMG indicates phagocytosis of highly aggregated
959 Aβ. **B**: In both, 3w/5w Aβ treated hiNS(+), Aβ co-localizes with hiMG cell bodies (see white
960 arrows). Only at 5w, hiMG appear to clear volumes of tissue from Aβ leaving dark shadows in the
961 Aβ staining pattern (see red arrows). **C**: Conjugation of Aβ oligomers with pHrodo green (pHrodo-
962 Aβ) confirms functional phagocytosis of Aβ in hiMG. Successful microglial uptake of pHrodo-Aβ
963 was first tested in 2D hiMG (left). 3w Aβ hiNS(+) were treated for 1w with pHrodo-Aβ to confirm

964 microglial Aβ phagocytosis in 3D. Additional co-staining for IBA1 and GFAP reveals that microglia
965 are the main cell type phagocytosing Aβ in hiNS (right) (N=6 IBA1 co-stainings; N=3 GFAP co-
966 stainings).

967 **Figure S5:** Electrophysiological properties of hiMG in 3w and 5w Aβ hiNS(+). **A**: Current-voltage
968 relationship of hiMG ranging from -150 to +50 mV after chronic Aβ treatment appears similar to
969 hiMG from ctrl hiNS(+) with no significant increase in outward or inward currents. **B**: Reversal
970 potentials of hiMG do not differ between treatment groups indicating membrane potentials of ~-
971 40 mV. **c**: Membrane capacitance of hiMG was significantly increased in hiMG of 5w Aβ hiNS(+)
972 indicating potentially larger cell sizes with prolonged Aβ treatment (ctrl, 3w Aβ, 5w Aβ hiNS(+):
973 N=9 each).

974 **Figure S6**: Top 10 most significant DEGs per subcluster of hiMG from 5w Aβ hiNS(+) displayed
975 in a heatmap.

976

977 **References**


978 1. Guerreiro, R., Wojtas, A., Bras, J., Carrasquillo, M., Rogaeva, E., Majounie, E., Cruchaga, C., Sassi,
979 C., Kauwe, J.S., Younkin, S., et al. (2013). TREM2 variants in Alzheimer's disease. N Engl J Med *368*,
980 117-127. 10.1056/NEJMoa1211851.
981 2. Zhang, Y., Chen, H., Li, R., Sterling, K., and Song, W. (2023). Amyloid beta-based therapy for
982 Alzheimer's disease: challenges, successes and future. Signal Transduct Target Ther *8*, 248.
983 10.1038/s41392-023-01484-7.
984 3. Leisher, S., Bohorquez, A., Gay, M., Garcia, V., Jones, R., Baldaranov, D., and Rafii, M.S. (2023).
985 Amyloid-Lowering Monoclonal Antibodies for the Treatment of Early Alzheimer's Disease. CNS
986 Drugs *37*, 671-677. 10.1007/s40263-023-01021-8.
987 4. Piccioni, G., Mango, D., Saidi, A., Corbo, M., and Nistico, R. (2021). Targeting Microglia-Synapse
988 Interactions in Alzheimer's Disease. Int J Mol Sci *22*. 10.3390/ijms22052342.
989 5. Fernandez-Calle, R., Konings, S.C., Frontinan-Rubio, J., Garcia-Revilla, J., Camprubi-Ferrer, L.,
990 Svensson, M., Martinson, I., Boza-Serrano, A., Venero, J.L., Nielsen, H.M., et al. (2022). APOE in the
991 bullseye of neurodegenerative diseases: impact of the APOE genotype in Alzheimer's disease
992 pathology and brain diseases. Mol Neurodegener *17*, 62. 10.1186/s13024-022-00566-4.
993 6. Grubman, A., Chew, G., Ouyang, J.F., Sun, G., Choo, X.Y., McLean, C., Simmons, R.K., Buckberry, S.,
994 Vargas-Landin, D.B., Poppe, D., et al. (2019). A single-cell atlas of entorhinal cortex from individuals
995 with Alzheimer's disease reveals cell-type-specific gene expression regulation. Nat Neurosci *22*,
996 2087-2097. 10.1038/s41593-019-0539-4.
997 7. Sadick, J.S., O'Dea, M.R., Hasel, P., Dykstra, T., Faustin, A., and Liddelow, S.A. (2022). Astrocytes
998 and oligodendrocytes undergo subtype-specific transcriptional changes in Alzheimer's disease.
999 Neuron *110*, 1788-1805 e1710. 10.1016/j.neuron.2022.03.008.
1000 8. Gao, C., Shen, X., Tan, Y., and Chen, S. (2022). Pathogenesis, therapeutic strategies and biomarker
1001 development based on "omics" analysis related to microglia in Alzheimer's disease. J
1002 Neuroinflammation *19*, 215. 10.1186/s12974-022-02580-1.
1003 9. Drummond, E., and Wisniewski, T. (2017). Alzheimer's disease: experimental models and reality.
1004 Acta Neuropathol *133*, 155-175. 10.1007/s00401-016-1662-x.
1005 10. Barak, M., Fedorova, V., Pospisilova, V., Raska, J., Vochyanova, S., Sedmik, J., Hribkova, H., Klimova,
1006 H., Vanova, T., and Bohaciakova, D. (2022). Human iPSC-Derived Neural Models for Studying
1007 Alzheimer's Disease: from Neural Stem Cells to Cerebral Organoids. Stem Cell Rev Rep *18*, 792-
1008 820. 10.1007/s12015-021-10254-3.
1009 11. Papaspyropoulos, A., Tsolaki, M., Foroglou, N., and Pantazaki, A.A. (2020). Modeling and Targeting
1010 Alzheimer's Disease With Organoids. Front Pharmacol *11*, 396. 10.3389/fphar.2020.00396.
1011 12. Sreenivasamurthy, S., Laul, M., Zhao, N., Kim, T., and Zhu, D. (2023). Current progress of cerebral
1012 organoids for modeling Alzheimer's disease origins and mechanisms. Bioeng Transl Med *8*,
1013 e10378. 10.1002/btm2.10378.
1014 13. Choi, S.H., Kim, Y.H., Quinti, L., Tanzi, R.E., and Kim, D.Y. (2016). 3D culture models of Alzheimer's
1015 disease: a road map to a "cure-in-a-dish". Mol Neurodegener *11*, 75. 10.1186/s13024-016-0139-
1016 7.
1017 14. Hernandez-Sapiens, M.A., Reza-Zaldivar, E.E., Cevallos, R.R., Marquez-Aguirre, A.L., Gazarian, K.,
1018 and Canales-Aguirre, A.A. (2020). A Three-Dimensional Alzheimer's Disease Cell Culture Model
1019 Using iPSC-Derived Neurons Carrying A246E Mutation in PSEN1. Front Cell Neurosci *14*, 151.
1020 10.3389/fncel.2020.00151.
1021 15. Jorfi, M., Park, J., Hall, C.K., Lin, C.J., Chen, M., von Maydell, D., Kruskop, J.M., Kang, B., Choi, Y.,
1022 Prokopenko, D., et al. (2023). Infiltrating CD8(+) T cells exacerbate Alzheimer's disease pathology

in a 3D human neuroimmune axis model. Nat Neurosci *26*, 1489-1504. 10.1038/s41593-023-01415-3.

16. Kim, Y.H., Choi, S.H., D'Avanzo, C., Hebisch, M., Sliwinski, C., Bylykbashi, E., Washicosky, K.J., Klee, J.B., Brustle, O., Tanzi, R.E., and Kim, D.Y. (2015). A 3D human neural cell culture system for modeling Alzheimer's disease. Nat Protoc *10*, 985-1006. 10.1038/nprot.2015.065.
17. Kwak, S.S., Washicosky, K.J., Brand, E., von Maydell, D., Aronson, J., Kim, S., Capen, D.E., Cetinbas, M., Sadreyev, R., Ning, S., et al. (2020). Amyloid-beta42/40 ratio drives tau pathology in 3D human neural cell culture models of Alzheimer's disease. Nat Commun *11*, 1377. 10.1038/s41467-020-15120-3.
18. Poli, D., Magliaro, C., and Ahluwalia, A. (2019). Experimental and Computational Methods for the Study of Cerebral Organoids: A Review. Front Neurosci *13*, 162. 10.3389/fnins.2019.00162.
19. Hanson, G.T., Aggeler, R., Oglesbee, D., Cannon, M., Capaldi, R.A., Tsien, R.Y., and Remington, S.J. (2004). Investigating mitochondrial redox potential with redox-sensitive green fluorescent protein indicators. J Biol Chem *279*, 13044-13053. 10.1074/jbc.M312846200.
20. Wendt, S., Johnson, S., Weilinger, N.L., Groten, C., Sorrentino, S., Frew, J., Yang, L., Choi, H.B., Nygaard, H.B., and MacVicar, B.A. (2022). Simultaneous imaging of redox states in dystrophic neurites and microglia at Abeta plaques indicate lysosome accumulation not microglia correlate with increased oxidative stress. Redox Biol *56*, 102448. 10.1016/j.redox.2022.102448.
21. Hao, Y., Hao, S., Andersen-Nissen, E., Mauck, W.M., 3rd, Zheng, S., Butler, A., Lee, M.J., Wilk, A.J., Darby, C., Zager, M., et al. (2021). Integrated analysis of multimodal single-cell data. Cell *184*, 3573-3587 e3529. 10.1016/j.cell.2021.04.048.
22. Lun, A.T., McCarthy, D.J., and Marioni, J.C. (2016). A step-by-step workflow for low-level analysis of single-cell RNA-seq data with Bioconductor. F1000Res *5*, 2122. 10.12688/f1000research.9501.2.
23. Yuzwa, S.A., Borrett, M.J., Innes, B.T., Voronova, A., Ketela, T., Kaplan, D.R., Bader, G.D., and Miller, F.D. (2017). Developmental Emergence of Adult Neural Stem Cells as Revealed by Single-Cell Transcriptional Profiling. Cell Rep *21*, 3970-3986. 10.1016/j.celrep.2017.12.017.
24. Borrett, M.J., Innes, B.T., Tahmasian, N., Bader, G.D., Kaplan, D.R., and Miller, F.D. (2022). A Shared Transcriptional Identity for Forebrain and Dentate Gyrus Neural Stem Cells from Embryogenesis to Adulthood. eNeuro *9*. 10.1523/ENEURO.0271-21.2021.
25. Borrett, M.J., Innes, B.T., Jeong, D., Tahmasian, N., Storer, M.A., Bader, G.D., Kaplan, D.R., and Miller, F.D. (2020). Single-Cell Profiling Shows Murine Forebrain Neural Stem Cells Reacquire a Developmental State when Activated for Adult Neurogenesis. Cell Rep *32*, 108022. 10.1016/j.celrep.2020.108022.
26. Arjun McKinney, A., Petrova, R., and Panagiotakos, G. (2022). Calcium and activity-dependent signaling in the developing cerebral cortex. Development *149*. 10.1242/dev.198853.
27. Namiki, S., Norimoto, H., Kobayashi, C., Nakatani, K., Matsuki, N., and Ikegaya, Y. (2013). Layer III neurons control synchronized waves in the immature cerebral cortex. J Neurosci *33*, 987-1001. 10.1523/JNEUROSCI.2522-12.2013.
28. Boucsein, C., Zacharias, R., Farber, K., Pavlovic, S., Hanisch, U.K., and Kettenmann, H. (2003). Purinergic receptors on microglial cells: functional expression in acute brain slices and modulation of microglial activation in vitro. Eur J Neurosci *17*, 2267-2276. 10.1046/j.1460-9568.2003.02663.x.
29. Wendt, S., Maricos, M., Vana, N., Meyer, N., Guneykaya, D., Semtner, M., and Kettenmann, H. (2017). Changes in phagocytosis and potassium channel activity in microglia of 5xFAD mice indicate alterations in purinergic signaling in a mouse model of Alzheimer's disease. Neurobiol Aging *58*, 41-53. 10.1016/j.neurobiolaging.2017.05.027.

1069 30. Wendt, S., Wogram, E., Korvers, L., and Kettenmann, H. (2016). Experimental Cortical Spreading
1070 Depression Induces NMDA Receptor Dependent Potassium Currents in Microglia. J Neurosci *36*,
1071 6165-6174. 10.1523/JNEUROSCI.4498-15.2016.
1072 31. Zhang, G., Wang, Z., Hu, H., Zhao, M., and Sun, L. (2021). Microglia in Alzheimer's Disease: A Target
1073 for Therapeutic Intervention. Front Cell Neurosci *15*, 749587. 10.3389/fncel.2021.749587.
1074 32. Gao, C., Jiang, J., Tan, Y., and Chen, S. (2023). Microglia in neurodegenerative diseases: mechanism
1075 and potential therapeutic targets. Signal Transduct Target Ther *8*, 359. 10.1038/s41392-023-
1076 01588-0.
1077 33. Hatami, A., Albay, R., 3rd, Monjazeb, S., Milton, S., and Glabe, C. (2014). Monoclonal antibodies
1078 against Abeta42 fibrils distinguish multiple aggregation state polymorphisms in vitro and in
1079 Alzheimer disease brain. J Biol Chem *289*, 32131-32143. 10.1074/jbc.M114.594846.
1080 34. Jung, H., Lee, S.Y., Lim, S., Choi, H.R., Choi, Y., Kim, M., Kim, S., Lee, Y., Han, K.H., Chung, W.S., and
1081 Kim, C.H. (2022). Anti-inflammatory clearance of amyloid-beta by a chimeric Gas6 fusion protein.
1082 Nat Med *28*, 1802-1812. 10.1038/s41591-022-01926-9.
1083 35. Keren-Shaul, H., Spinrad, A., Weiner, A., Matcovitch-Natan, O., Dvir-Szternfeld, R., Ulland, T.K.,
1084 David, E., Baruch, K., Lara-Astaiso, D., Toth, B., et al. (2017). A Unique Microglia Type Associated
1085 with Restricting Development of Alzheimer's Disease. Cell *169*, 1276-1290 e1217.
1086 10.1016/j.cell.2017.05.018.
1087 36. Raulin, A.C., Doss, S.V., Trottier, Z.A., Ikezu, T.C., Bu, G., and Liu, C.C. (2022). ApoE in Alzheimer's
1088 disease: pathophysiology and therapeutic strategies. Mol Neurodegener *17*, 72. 10.1186/s13024-
1089 022-00574-4.
1090 37. Delhaye, M., LeDue, J., Robinson, K., Xu, Q., Zhang, Q., Oku, S., Zhang, P., and Craig, A.M. (2024).
1091 Adaptation of Magnified Analysis of the Proteome for Excitatory Synaptic Proteins in Varied
1092 Samples and Evaluation of Cell Type-Specific Distributions. J Neurosci *44*.
1093 10.1523/JNEUROSCI.1291-23.2024.
1094 38. Kuga, N., Sasaki, T., Takahara, Y., Matsuki, N., and Ikegaya, Y. (2011). Large-scale calcium waves
1095 traveling through astrocytic networks in vivo. J Neurosci *31*, 2607-2614.
1096 10.1523/JNEUROSCI.5319-10.2011.
1097 39. Yuryev, M., Pellegrino, C., Jokinen, V., Andriichuk, L., Khirug, S., Khiroug, L., and Rivera, C. (2015).
1098 In vivo Calcium Imaging of Evoked Calcium Waves in the Embryonic Cortex. Front Cell Neurosci *9*,
1099 500. 10.3389/fncel.2015.00500.
1100 40. Xiang, Y., Tanaka, Y., Patterson, B., Kang, Y.J., Govindaiah, G., Roselaar, N., Cakir, B., Kim, K.Y.,
1101 Lombroso, A.P., Hwang, S.M., et al. (2017). Fusion of Regionally Specified hPSC-Derived Organoids
1102 Models Human Brain Development and Interneuron Migration. Cell Stem Cell *21*, 383-398 e387.
1103 10.1016/j.stem.2017.07.007.
1104 41. Woodruff, G., Phillips, N., Carromeu, C., Guicherit, O., White, A., Johnson, M., Zanella, F., Anson,
1105 B., Lovenberg, T., Bonaventure, P., and Harrington, A.W. (2020). Screening for modulators of neural
1106 network activity in 3D human iPSC-derived cortical spheroids. PLoS One *15*, e0240991.
1107 10.1371/journal.pone.0240991.
1108 42. Michell-Robinson, M.A., Touil, H., Healy, L.M., Owen, D.R., Durafourt, B.A., Bar-Or, A., Antel, J.P.,
1109 and Moore, C.S. (2015). Roles of microglia in brain development, tissue maintenance and repair.
1110 Brain *138*, 1138-1159. 10.1093/brain/awv066.
1111 43. Park, J., Wetzel, I., Marriott, I., Dreau, D., D'Avanzo, C., Kim, D.Y., Tanzi, R.E., and Cho, H. (2018). A
1112 3D human triculture system modeling neurodegeneration and neuroinflammation in Alzheimer's
1113 disease. Nat Neurosci *21*, 941-951. 10.1038/s41593-018-0175-4.
1114 44. Rifat, A., Ossola, B., Burli, R.W., Dawson, L.A., Brice, N.L., Rowland, A., Lizio, M., Xu, X., Page, K.,
1115 Fidzinski, P., et al. (2024). Differential contribution of THIK-1 K(+) channels and P2X7 receptors to

ATP-mediated neuroinflammation by human microglia. J Neuroinflammation *21*, 58. 10.1186/s12974-024-03042-6.

45. Golde, T.E. (2022). Alzheimer's disease - the journey of a healthy brain into organ failure. Mol Neurodegener *17*, 18. 10.1186/s13024-022-00523-1.

46. Misrani, A., Tabassum, S., and Yang, L. (2021). Mitochondrial Dysfunction and Oxidative Stress in Alzheimer's Disease. Front Aging Neurosci *13*, 617588. 10.3389/fnagi.2021.617588.

47. Huang, W.J., Zhang, X., and Chen, W.W. (2016). Role of oxidative stress in Alzheimer's disease. Biomed Rep *4*, 519-522. 10.3892/br.2016.630.

48. Fracassi, A., Marcatti, M., Zolochevska, O., Tabor, N., Woltjer, R., Moreno, S., and Taglialatela, G. (2021). Oxidative Damage and Antioxidant Response in Frontal Cortex of Demented and Nondemented Individuals with Alzheimer's Neuropathology. J Neurosci *41*, 538-554. 10.1523/JNEUROSCI.0295-20.2020.

49. Palop, J.J., and Mucke, L. (2010). Amyloid-beta-induced neuronal dysfunction in Alzheimer's disease: from synapses toward neural networks. Nat Neurosci *13*, 812-818. 10.1038/nn.2583.

50. Louneva, N., Cohen, J.W., Han, L.Y., Talbot, K., Wilson, R.S., Bennett, D.A., Trojanowski, J.Q., and Arnold, S.E. (2008). Caspase-3 is enriched in postsynaptic densities and increased in Alzheimer's disease. Am J Pathol *173*, 1488-1495. 10.2353/ajpath.2008.080434.

51. Stadelmann, C., Deckwerth, T.L., Srinivasan, A., Bancher, C., Bruck, W., Jellinger, K., and Lassmann, H. (1999). Activation of caspase-3 in single neurons and autophagic granules of granulovacuolar degeneration in Alzheimer's disease. Evidence for apoptotic cell death. Am J Pathol *155*, 1459-1466. 10.1016/S0002-9440(10)65460-0.

52. Goel, P., Chakrabarti, S., Goel, K., Bhutani, K., Chopra, T., and Bali, S. (2022). Neuronal cell death mechanisms in Alzheimer's disease: An insight. Front Mol Neurosci *15*, 937133. 10.3389/fnmol.2022.937133.

53. Hansen, D.V., Hanson, J.E., and Sheng, M. (2018). Microglia in Alzheimer's disease. J Cell Biol *217*, 459-472. 10.1083/jcb.201709069.

54. Leng, F., and Edison, P. (2021). Neuroinflammation and microglial activation in Alzheimer disease: where do we go from here? Nat Rev Neurol *17*, 157-172. 10.1038/s41582-020-00435-y.

55. Fan, Z., Brooks, D.J., Okello, A., and Edison, P. (2017). An early and late peak in microglial activation in Alzheimer's disease trajectory. Brain *140*, 792-803. 10.1093/brain/aww349.

56. Solito, E., and Sastre, M. (2012). Microglia function in Alzheimer's disease. Front Pharmacol *3*, 14. 10.3389/fphar.2012.00014.

57. Wyss-Coray, T. (2006). Inflammation in Alzheimer disease: driving force, bystander or beneficial response? Nat Med *12*, 1005-1015. 10.1038/nm1484.

58. Long, H.Z., Zhou, Z.W., Cheng, Y., Luo, H.Y., Li, F.J., Xu, S.G., and Gao, L.C. (2022). The Role of Microglia in Alzheimer's Disease From the Perspective of Immune Inflammation and Iron Metabolism. Front Aging Neurosci *14*, 888989. 10.3389/fnagi.2022.888989.

59. Rossol, M., Heine, H., Meusch, U., Quandt, D., Klein, C., Sweet, M.J., and Hauschildt, S. (2011). LPS-induced cytokine production in human monocytes and macrophages. Crit Rev Immunol *31*, 379-446. 10.1615/critrevimmunol.v31.i5.20.

60. Erta, M., Quintana, A., and Hidalgo, J. (2012). Interleukin-6, a major cytokine in the central nervous system. Int J Biol Sci *8*, 1254-1266. 10.7150/ijbs.4679.

61. Feng, Q., Wang, Y.I., and Yang, Y. (2015). Neuroprotective effect of interleukin-6 in a rat model of cerebral ischemia. Exp Ther Med *9*, 1695-1701. 10.3892/etm.2015.2363.

62. Andreadou, M., Ingelfinger, F., De Feo, D., Cramer, T.L.M., Tuzlak, S., Friebel, E., Schreiner, B., Eede, P., Schneeberger, S., Geesdorf, M., et al. (2023). IL-12 sensing in neurons induces neuroprotective CNS tissue adaptation and attenuates neuroinflammation in mice. Nat Neurosci *26*, 1701-1712. 10.1038/s41593-023-01435-z.

63. Yang, H.S., Zhang, C., Carlyle, B.C., Zhen, S.Y., Trombetta, B.A., Schultz, A.P., Pruzin, J.J., Fitzpatrick, C.D., Yau, W.W., Kirn, D.R., et al. (2022). Plasma IL-12/IFN-gamma axis predicts cognitive trajectories in cognitively unimpaired older adults. Alzheimers Dement *18*, 645-653. 10.1002/alz.12399.
64. Vom Berg, J., Prokop, S., Miller, K.R., Obst, J., Kalin, R.E., Lopategui-Cabezas, I., Wegner, A., Mair, F., Schipke, C.G., Peters, O., et al. (2012). Inhibition of IL-12/IL-23 signaling reduces Alzheimer's disease-like pathology and cognitive decline. Nat Med *18*, 1812-1819. 10.1038/nm.2965.
65. Dolan, M.J., Therrien, M., Jereb, S., Kamath, T., Gazestani, V., Atkeson, T., Marsh, S.E., Goeva, A., Lojek, N.M., Murphy, S., et al. (2023). Exposure of iPSC-derived human microglia to brain substrates enables the generation and manipulation of diverse transcriptional states in vitro. Nat Immunol *24*, 1382-1390. 10.1038/s41590-023-01558-2.
66. Abud, E.M., Ramirez, R.N., Martinez, E.S., Healy, L.M., Nguyen, C.H.H., Newman, S.A., Yeromin, A.V., Scarfone, V.M., Marsh, S.E., Fimbres, C., et al. (2017). iPSC-Derived Human Microglia-like Cells to Study Neurological Diseases. Neuron *94*, 278-293 e279. 10.1016/j.neuron.2017.03.042.
67. Takata, M., Nishimura, K., Harada, K., Iwasaki, R., Ando, M., Yamada, S., Ginhoux, F., and Takata, K. (2023). Analysis of Abeta-induced neurotoxicity and microglial responses in simple two- and three-dimensional human iPSC-derived cortical culture systems. Tissue Cell *81*, 102023. 10.1016/j.tice.2023.102023.
68. Alkhalifa, A.E., Al-Ghraiybah, N.F., Odum, J., Shunnarah, J.G., Austin, N., and Kaddoumi, A. (2023). Blood-Brain Barrier Breakdown in Alzheimer's Disease: Mechanisms and Targeted Strategies. Int J Mol Sci *24*. 10.3390/ijms242216288.
69. Chun, H., and Lee, C.J. (2018). Reactive astrocytes in Alzheimer's disease: A double-edged sword. Neurosci Res *126*, 44-52. 10.1016/j.neures.2017.11.012.
70. Yamazaki, Y., Zhao, N., Caulfield, T.R., Liu, C.C., and Bu, G. (2019). Apolipoprotein E and Alzheimer disease: pathobiology and targeting strategies. Nat Rev Neurol *15*, 501-518. 10.1038/s41582-019-0228-7.
71. Chen, Y., Strickland, M.R., Soranno, A., and Holtzman, D.M. (2021). Apolipoprotein E: Structural Insights and Links to Alzheimer Disease Pathogenesis. Neuron *109*, 205-221. 10.1016/j.neuron.2020.10.008.
72. Sun, M., You, H., Hu, X., Luo, Y., Zhang, Z., Song, Y., An, J., and Lu, H. (2023). Microglia-Astrocyte Interaction in Neural Development and Neural Pathogenesis. Cells *12*. 10.3390/cells12151942.
73. Matejuk, A., and Ransohoff, R.M. (2020). Crosstalk Between Astrocytes and Microglia: An Overview. Front Immunol *11*, 1416. 10.3389/fimmu.2020.01416.
74. Zhang, H., Wu, L.M., and Wu, J. (2011). Cross-talk between apolipoprotein E and cytokines. Mediators Inflamm *2011*, 949072. 10.1155/2011/949072.
75. Shinohara, M., Tachibana, M., Kanekiyo, T., and Bu, G. (2017). Role of LRP1 in the pathogenesis of Alzheimer's disease: evidence from clinical and preclinical studies. J Lipid Res *58*, 1267-1281. 10.1194/jlr.R075796.
76. Liu, C.C., Hu, J., Zhao, N., Wang, J., Wang, N., Cirrito, J.R., Kanekiyo, T., Holtzman, D.M., and Bu, G. (2017). Astrocytic LRP1 Mediates Brain Abeta Clearance and Impacts Amyloid Deposition. J Neurosci *37*, 4023-4031. 10.1523/JNEUROSCI.3442-16.2017.
77. Habib, N., McCabe, C., Medina, S., Varshavsky, M., Kitsberg, D., Dvir-Szternfeld, R., Green, G., Dionne, D., Nguyen, L., Marshall, J.L., et al. (2020). Disease-associated astrocytes in Alzheimer's disease and aging. Nat Neurosci *23*, 701-706. 10.1038/s41593-020-0624-8.
78. Foster, E.M., Dangla-Valls, A., Lovestone, S., Ribe, E.M., and Buckley, N.J. (2019). Clusterin in Alzheimer's Disease: Mechanisms, Genetics, and Lessons From Other Pathologies. Front Neurosci *13*, 164. 10.3389/fnins.2019.00164.

1211 79. Kamphuis, W., Kooijman, L., Orre, M., Stassen, O., Pekny, M., and Hol, E.M. (2015). GFAP and
1212 vimentin deficiency alters gene expression in astrocytes and microglia in wild-type mice and
1213 changes the transcriptional response of reactive glia in mouse model for Alzheimer's disease. Glia
1214 *63*, 1036-1056. 10.1002/glia.22800.
1215 80. Drummond, E., Nayak, S., Faustin, A., Pires, G., Hickman, R.A., Askenazi, M., Cohen, M., Haldiman,
1216 T., Kim, C., Han, X., et al. (2017). Proteomic differences in amyloid plaques in rapidly progressive
1217 and sporadic Alzheimer's disease. Acta Neuropathol *133*, 933-954. 10.1007/s00401-017-1691-0.
1218 81. Kim, J., Yoo, I.D., Lim, J., and Moon, J.S. (2024). Pathological phenotypes of astrocytes in
1219 Alzheimer's disease. Exp Mol Med *56*, 95-99. 10.1038/s12276-023-01148-0.
1220 82. Bakken, T.E., Hodge, R.D., Miller, J.A., Yao, Z., Nguyen, T.N., Aevermann, B., Barkan, E., Bertagnolli,
1221 D., Casper, T., Dee, N., et al. (2018). Single-nucleus and single-cell transcriptomes compared in
1222 matched cortical cell types. PLoS One *13*, e0209648. 10.1371/journal.pone.0209648.
1223 83. Mathys, H., Davila-Velderrain, J., Peng, Z., Gao, F., Mohammadi, S., Young, J.Z., Menon, M., He, L.,
1224 Abdurrob, F., Jiang, X., et al. (2019). Single-cell transcriptomic analysis of Alzheimer's disease.
1225 Nature *570*, 332-337. 10.1038/s41586-019-1195-2.
1226 84. Kamphuis, W., Middeldorp, J., Kooijman, L., Sluijs, J.A., Kooi, E.J., Moeton, M., Freriks, M., Mizee,
1227 M.R., and Hol, E.M. (2014). Glial fibrillary acidic protein isoform expression in plaque related
1228 astrogliosis in Alzheimer's disease. Neurobiol Aging *35*, 492-510.
1229 10.1016/j.neurobiolaging.2013.09.035.
1230 85. Jiwaji, Z., Tiwari, S.S., Aviles-Reyes, R.X., Hooley, M., Hampton, D., Torvell, M., Johnson, D.A.,
1231 McQueen, J., Baxter, P., Sabari-Sankar, K., et al. (2022). Reactive astrocytes acquire
1232 neuroprotective as well as deleterious signatures in response to Tau and Ass pathology. Nat
1233 Commun *13*, 135. 10.1038/s41467-021-27702-w.
1234 86. Ganne, A., Balasubramaniam, M., Griffin, W.S.T., Shmookler Reis, R.J., and Ayyadevara, S. (2022).
1235 Glial Fibrillary Acidic Protein: A Biomarker and Drug Target for Alzheimer's Disease. Pharmaceutics
1236 *14*. 10.3390/pharmaceutics14071354.
1237 87. Dai, D.L., Li, M., and Lee, E.B. (2023). Human Alzheimer's disease reactive astrocytes exhibit a loss
1238 of homeostastic gene expression. Acta Neuropathol Commun *11*, 127. 10.1186/s40478-023-
1239 01624-8.
1240 88. D'Ezio, V., Colasanti, M., and Persichini, T. (2021). Amyloid-beta 25-35 Induces Neurotoxicity
1241 through the Up-Regulation of Astrocytic System X(c)(). Antioxidants (Basel) *10*.
1242 10.3390/antiox10111685.
1243 89. Cui, X., Zong, S., Song, W., Wang, C., Liu, Y., Zhang, L., Xia, P., Wang, X., Zhao, H., Wang, L., and Lu,
1244 Z. (2023). Omaveloxolone ameliorates cognitive dysfunction in APP/PS1 mice by stabilizing the
1245 STAT3 pathway. Life Sci *335*, 122261. 10.1016/j.lfs.2023.122261.
1246 90. Frew, J., Baradaran-Heravi, A., Balgi, A.D., Wu, X., Yan, T.D., Arns, S., Shidmoossavee, F.S., Tan, J.,
1247 Jaquith, J.B., Jansen-West, K.R., et al. (2020). Premature termination codon readthrough
1248 upregulates progranulin expression and improves lysosomal function in preclinical models of GRN
1249 deficiency. Mol Neurodegener *15*, 21. 10.1186/s13024-020-00369-5.
1250 91. Lee, C., Frew, J., Weilinger, N.L., Wendt, S., Cai, W., Sorrentino, S., Wu, X., MacVicar, B.A., Willerth,
1251 S.M., and Nygaard, H.B. (2023). hiPSC-derived GRN-deficient astrocytes delay spiking activity of
1252 developing neurons. Neurobiol Dis *181*, 106124. 10.1016/j.nbd.2023.106124.
1253 92. Rose, S.E., Frankowski, H., Knupp, A., Berry, B.J., Martinez, R., Dinh, S.Q., Bruner, L.T., Willis, S.L.,
1254 Crane, P.K., Larson, E.B., et al. (2018). Leptomeninges-Derived Induced Pluripotent Stem Cells and
1255 Directly Converted Neurons From Autopsy Cases With Varying Neuropathologic Backgrounds. J
1256 Neuropathol Exp Neurol *77*, 353-360. 10.1093/jnen/nly013.
1257 93. Wang, Y., DelRosso, N.V., Vaidyanathan, T.V., Cahill, M.K., Reitman, M.E., Pittolo, S., Mi, X., Yu, G.,
1258 and Poskanzer, K.E. (2019). Accurate quantification of astrocyte and neurotransmitter

1259 fluorescence dynamics for single-cell and population-level physiology. Nat Neurosci *22*, 1936-
1260 1944. 10.1038/s41593-019-0492-2.
1261 94. Ku, T., Swaney, J., Park, J.Y., Albanese, A., Murray, E., Cho, J.H., Park, Y.G., Mangena, V., Chen, J.,
1262 and Chung, K. (2016). Multiplexed and scalable super-resolution imaging of three-dimensional
1263 protein localization in size-adjustable tissues. Nat Biotechnol *34*, 973-981. 10.1038/nbt.3641.
1264 95. Raudvere, U., Kolberg, L., Kuzmin, I., Arak, T., Adler, P., Peterson, H., and Vilo, J. (2019). g:Profiler:
1265 a web server for functional enrichment analysis and conversions of gene lists (2019 update).
1266 Nucleic Acids Res *47*, W191-W198. 10.1093/nar/gkz369.

1267

## Figures:

## Figure 1:

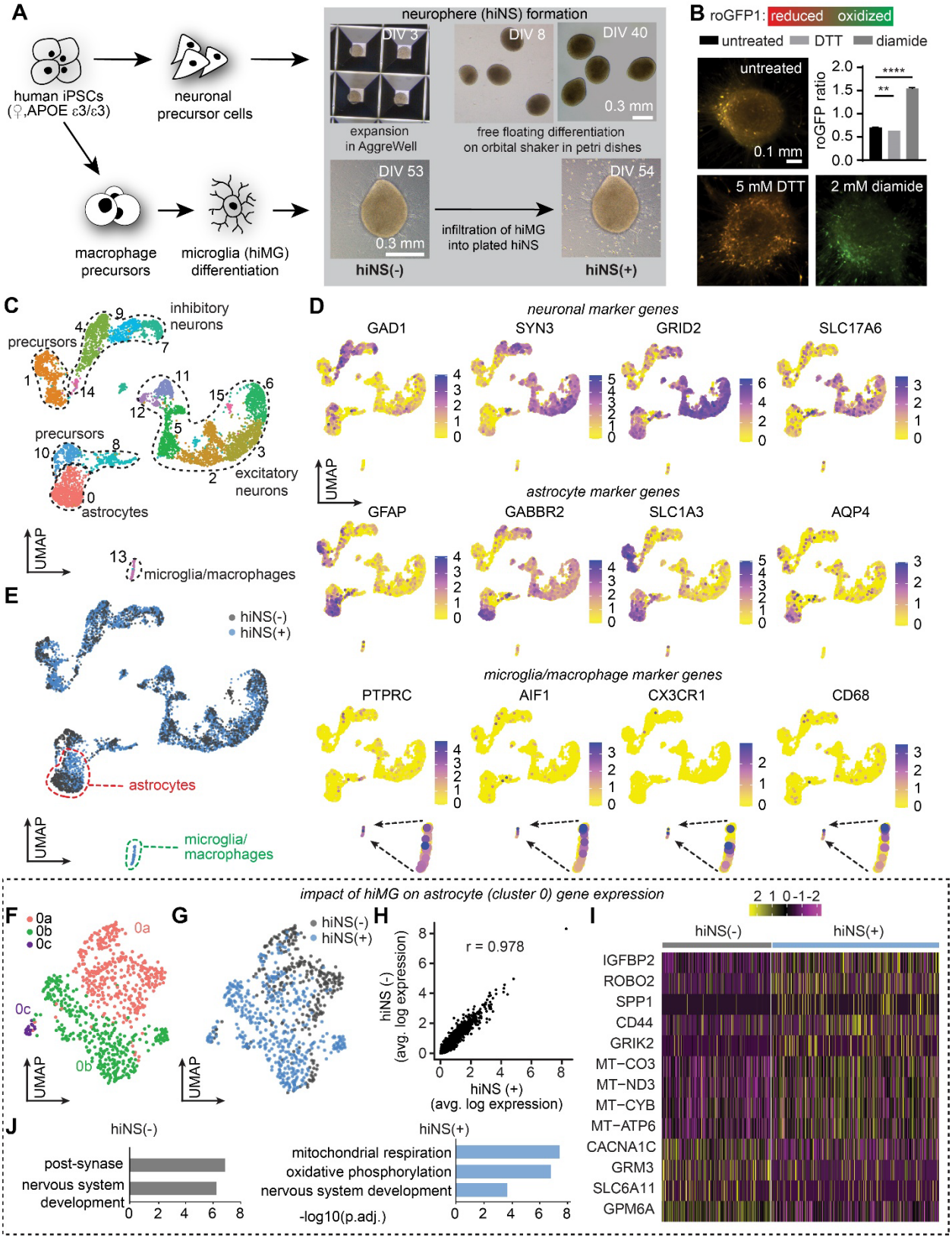

**Figure 2:**

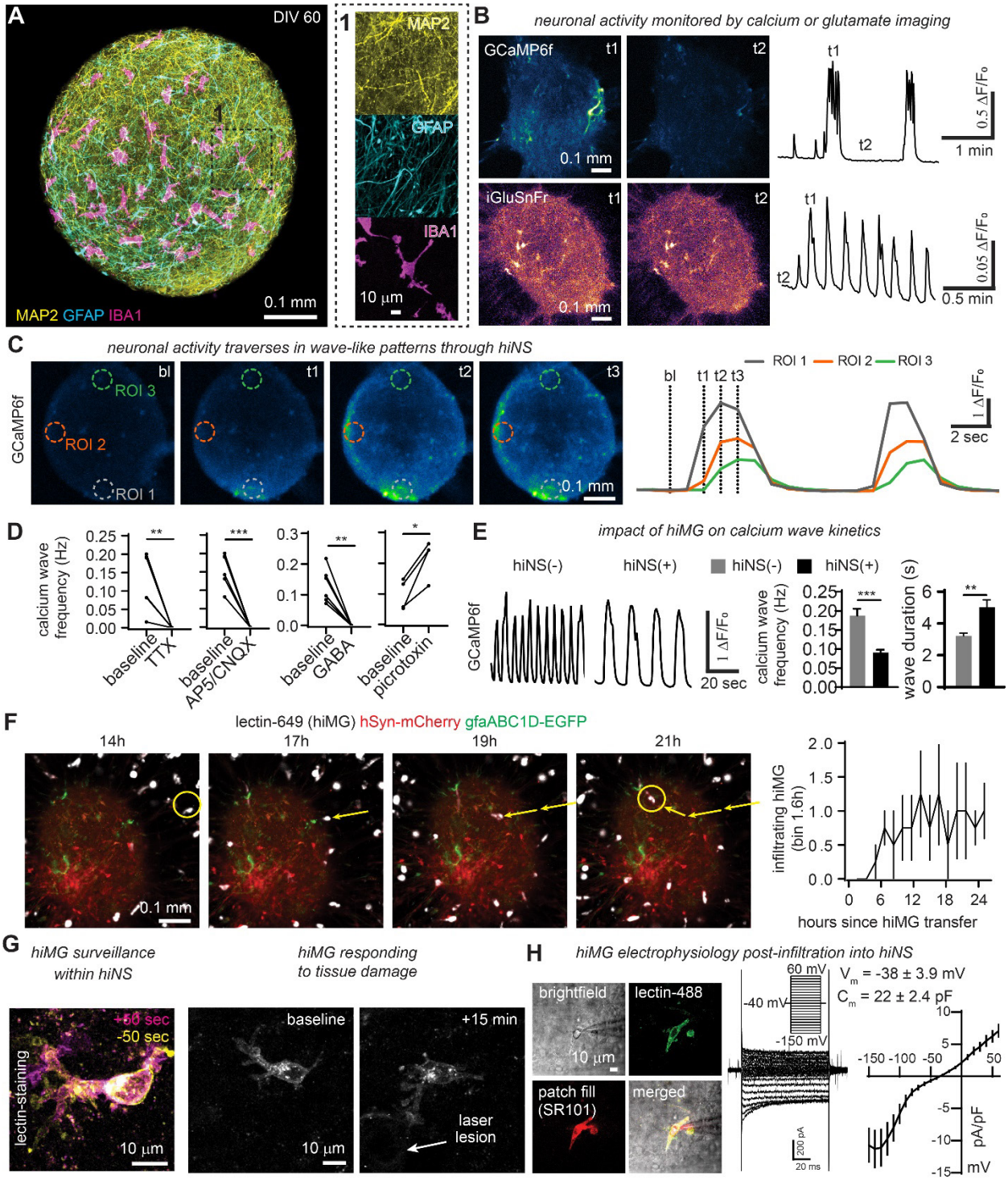
A
DIV 60
MAP2 GFAP IBA1
0.1 mm
1
MAP2
GFAP
IBA1
10 µm
B
neuronal activity monitored by calcium or glutamate imaging
GCaMP6f
t1
t2
0.1 mm
iGluSnFr
0.5 ΔF/Fo
1 min
0.05 ΔF/Fo
0.5 min
C
neuronal activity traverses in wave-like patterns through hiNS
GCaMP6f
bl
ROI 3
ROI 2
ROI 1
t3
ROI 1 ROI 2 ROI 3
1 ΔF/Fo
2 sec
D
calcium wave frequency (Hz)
baseline
TTX
AP5/CNQX
GABA
picrotoxin
E
impact of hiMG on calcium wave kinetics
hiNS(-)
hiNS(+)
20 sec
calcium wave frequency (Hz)
wave duration (s)
F
lectin-649 (hiMG) hSyn-mCherry gfaABC1D-EGFP
14h
17h
19h
21h
infiltrating hiMG (bin 1.6h)
hours since hiMG transfer
G
hiMG surveillance within hiNS
hiMG responding to tissue damage
+50 sec
-50 sec
lectin-staining
baseline
+15 min
laser lesion
H
hiMG electrophysiology post-infiltration into hiNS
brightfield
lectin-488
patch fill (SR101)
merged
60 mV
-40 mV
-150 mV
$V_m$ = -38 ± 3.9 mV
$C_m$ = 22 ± 2.4 pF
200 pA
20 ms
pA/pF
mV

**Figure 3:**

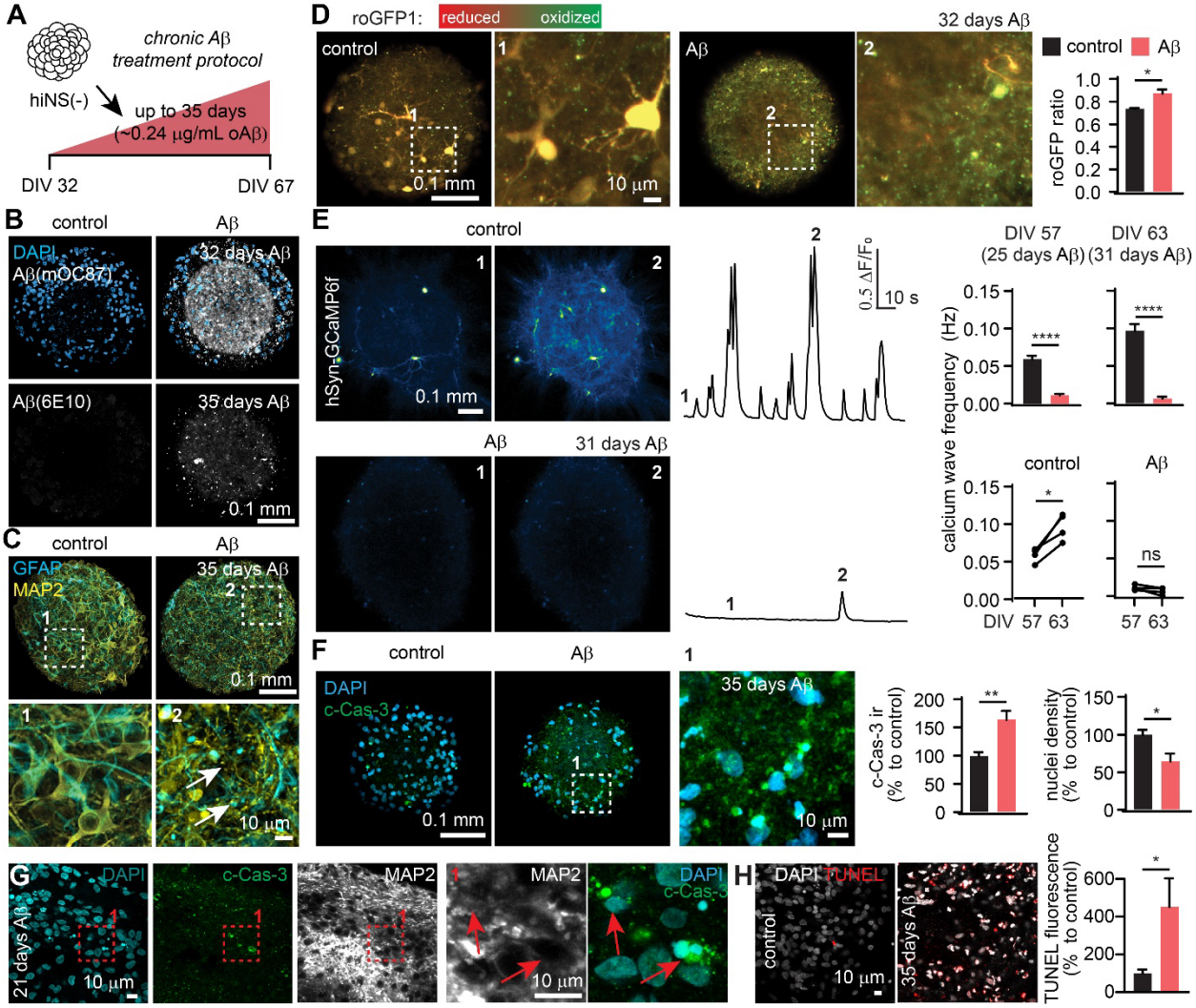
A
chronic Aβ treatment protocol
hiNS(-)
up to 35 days (~0.24 μg/mL oAβ)
DIV 32
DIV 67
B
control
Aβ
DAPI
Aβ(mOC87)
32 days Aβ
Aβ(6E10)
35 days Aβ
0.1 mm
C
control
Aβ
GFAP
MAP2
35 days Aβ
0.1 mm
10 μm
D
roGFP1:
reduced
oxidized
control
Aβ
32 days Aβ
0.1 mm
10 μm
roGFP ratio
E
control
hSyn-GCaMP6f
0.1 mm
0.5 ΔF/F₀
10 s
Aβ
31 days Aβ
DIV 57 (25 days Aβ)
DIV 63 (31 days Aβ)
calcium wave frequency (Hz)
****
ns
DIV 57 63
F
control
Aβ
DAPI
c-Cas-3
0.1 mm
35 days Aβ
10 μm
c-Cas-3 ir (% to control)
nuclei density (% to control)
G
DAPI
c-Cas-3
MAP2
21 days Aβ
10 μm
H
DAPI
TUNEL
control
35 days Aβ
10 μm
TUNEL fluorescence (% to control)

**Figure 4:**

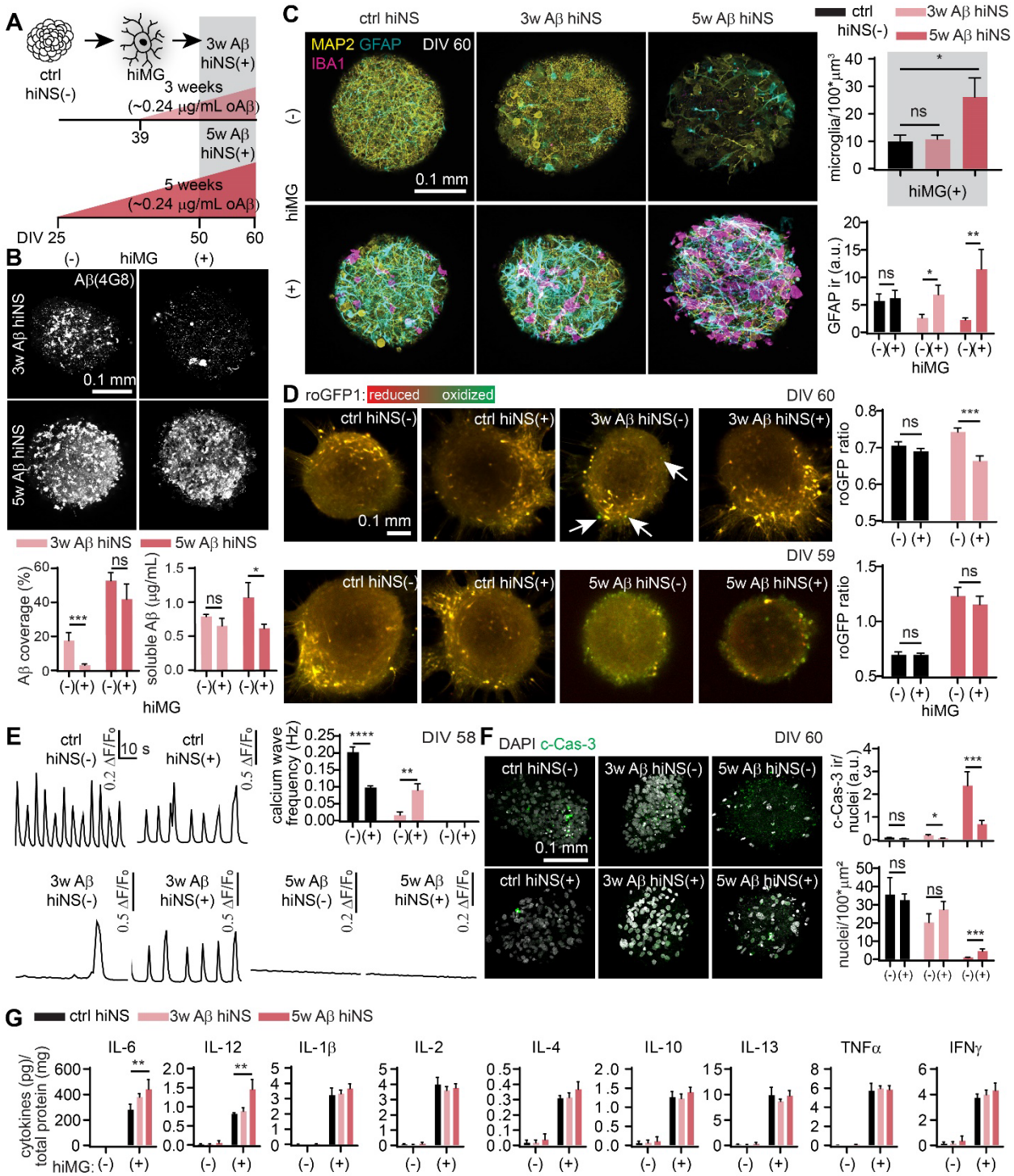
A
ctrl hiNS(-)
hiMG
3w Aβ hiNS(+)
3 weeks (~0.24 μg/mL oAβ)
39
5w Aβ hiNS(+)
5 weeks (~0.24 μg/mL oAβ)
DIV 25
50
60
B
(-) hiMG (+)
Aβ(4G8)
3w Aβ hiNS
5w Aβ hiNS
0.1 mm
3w Aβ hiNS
5w Aβ hiNS
Aβ coverage (%)
soluble Aβ (μg/mL)
hiMG
C
ctrl hiNS
3w Aβ hiNS
5w Aβ hiNS
MAP2 GFAP
IBA1
DIV 60
0.1 mm
hiMG
microglia/100*μm³
hiMG(+)
GFAP ir (a.u.)
D
roGFP1: reduced oxidized
DIV 60
ctrl hiNS(-)
ctrl hiNS(+)
3w Aβ hiNS(-)
3w Aβ hiNS(+)
0.1 mm
roGFP ratio
DIV 59
5w Aβ hiNS(-)
5w Aβ hiNS(+)
hiMG
E
ctrl hiNS(-)
ctrl hiNS(+)
10 s
0.2 ΔF/F₀
0.5 ΔF/F₀
calcium wave frequency (Hz)
DIV 58
3w Aβ hiNS(-)
3w Aβ hiNS(+)
5w Aβ hiNS(-)
5w Aβ hiNS(+)
F
DAPI c-Cas-3
DIV 60
ctrl hiNS(-)
3w Aβ hiNS(-)
5w Aβ hiNS(-)
ctrl hiNS(+)
3w Aβ hiNS(+)
5w Aβ hiNS(+)
0.1 mm
c-Cas-3 ir/nuclei (a.u.)
nuclei/100*μm²
G
ctrl hiNS
3w Aβ hiNS
5w Aβ hiNS
cytokines (pg)/total protein (mg)
IL-6
IL-12
IL-1β
IL-2
IL-4
IL-10
IL-13
TNFα
IFNγ
hiMG: (-) (+)

**Figure 5:**

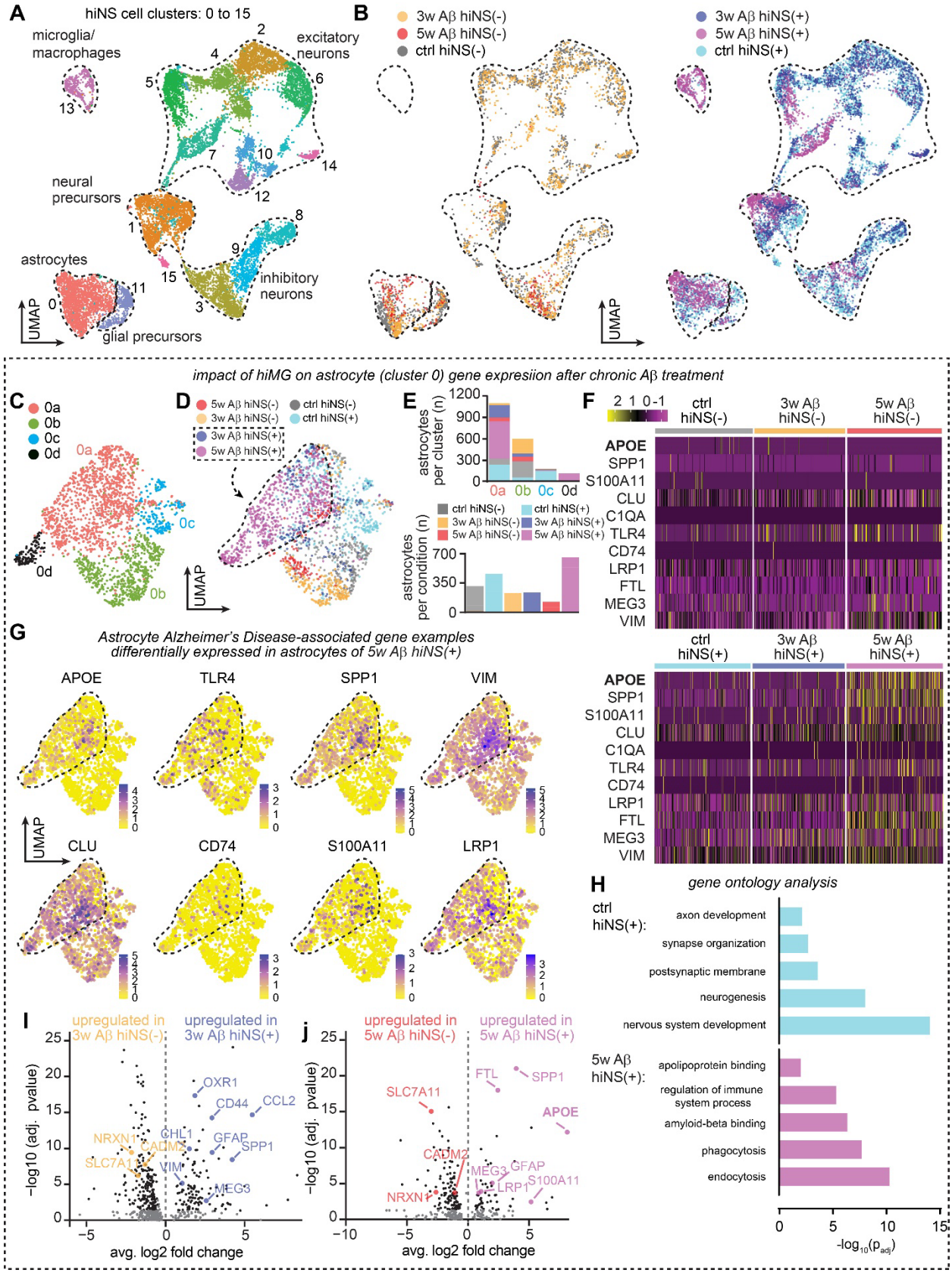
A
hiNS cell clusters: 0 to 15
microglia/ macrophages
excitatory neurons
neural precursors
astrocytes
inhibitory neurons
glial precursors
UMAP
B
3w Aβ hiNS(-)
5w Aβ hiNS(-)
ctrl hiNS(-)
3w Aβ hiNS(+)
5w Aβ hiNS(+)
ctrl hiNS(+)
impact of hiMG on astrocyte (cluster 0) gene expresiion after chronic Aβ treatment
C
0a
0b
0c
0d
D
E
astrocytes per cluster (n)
astrocytes per condition (n)
F
ctrl hiNS(-)
3w Aβ hiNS(-)
5w Aβ hiNS(-)
ctrl hiNS(+)
3w Aβ hiNS(+)
5w Aβ hiNS(+)
APOE
SPP1
S100A11
CLU
C1QA
TLR4
CD74
LRP1
FTL
MEG3
VIM
G
Astrocyte Alzheimer's Disease-associated gene examples differentially expressed in astrocytes of 5w Aβ hiNS(+)
APOE
TLR4
SPP1
VIM
CLU
CD74
S100A11
LRP1
H
gene ontology analysis
ctrl hiNS(+):
axon development
synapse organization
postsynaptic membrane
neurogenesis
nervous system development
5w Aβ hiNS(+):
apolipoprotein binding
regulation of immune system process
amyloid-beta binding
phagocytosis
endocytosis
-log10(padj)
I
upregulated in 3w Aβ hiNS(-)
upregulated in 3w Aβ hiNS(+)
OXR1
CD44
CCL2
NRXN1
CHL1
CADM2
GFAP
SPP1
SLC7A1
VIM
MEG3
-log10 (adj. pvalue)
avg. log2 fold change
J
upregulated in 5w Aβ hiNS(-)
upregulated in 5w Aβ hiNS(+)
FTL
SPP1
SLC7A11
APOE
CADM2
MEG3
GFAP
LRP1
S100A11
NRXN1

**Figure 6:**

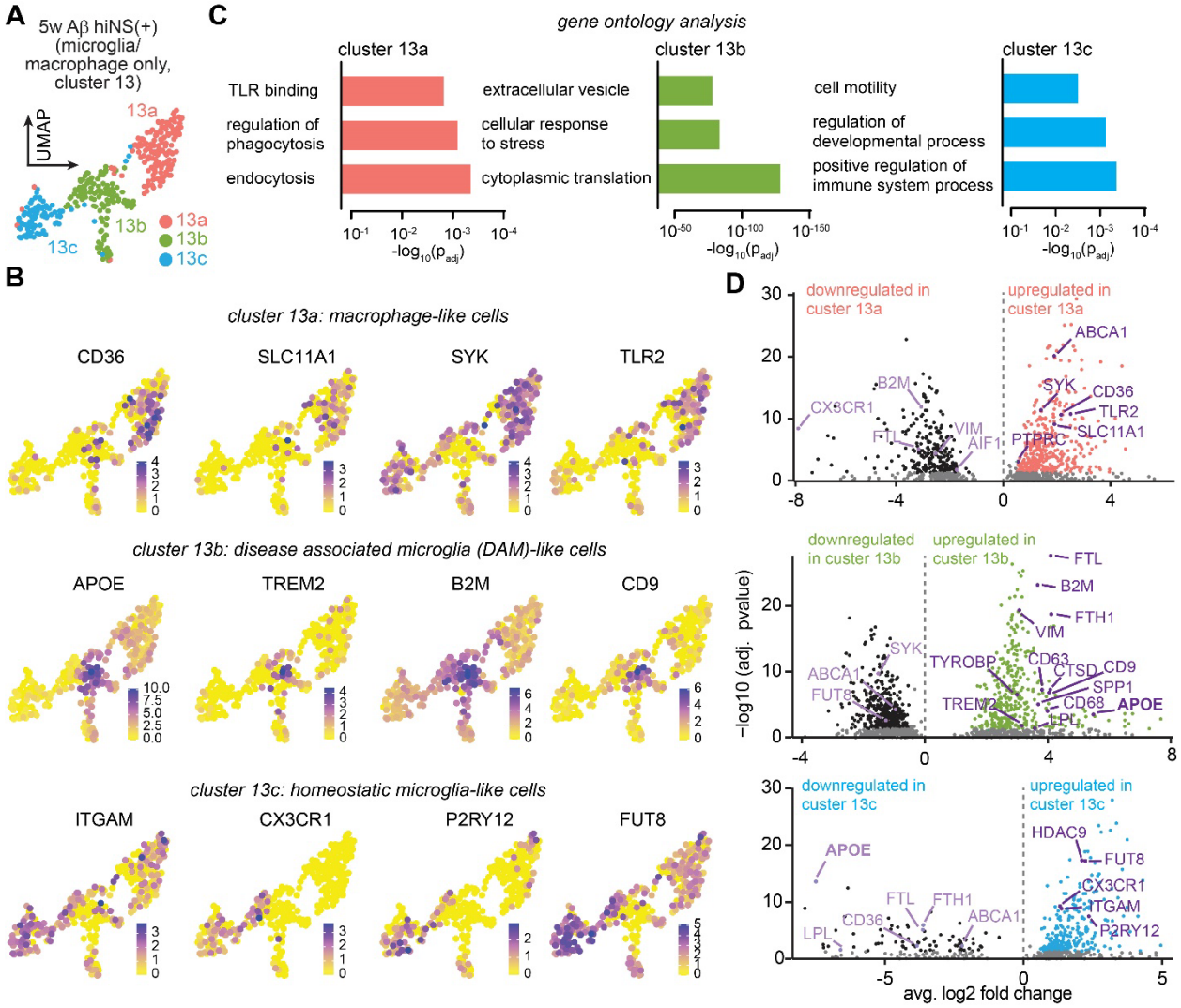
A
5w Aβ hiNS(+)
(microglia/
macrophage only,
cluster 13)
UMAP
13a
13b
13c
C
gene ontology analysis
cluster 13a
TLR binding
regulation of phagocytosis
endocytosis
cluster 13b
extracellular vesicle
cellular response to stress
cytoplasmic translation
cluster 13c
cell motility
regulation of developmental process
positive regulation of immune system process
-log10(padj)
B
cluster 13a: macrophage-like cells
CD36
SLC11A1
SYK
TLR2
cluster 13b: disease associated microglia (DAM)-like cells
APOE
TREM2
B2M
CD9
cluster 13c: homeostatic microglia-like cells
ITGAM
CX3CR1
P2RY12
FUT8
D
downregulated in custer 13a
upregulated in custer 13a
ABCA1
SYK
CD36
TLR2
SLC11A1
B2M
CX3CR1
FTL
VIM
AIF1
PTPRC
downregulated in custer 13b
upregulated in custer 13b
FTL
B2M
FTH1
VIM
SYK
TYROBP
CD63
CTSD
CD9
SPP1
CD68
APOE
LPL
ABCA1
FUT8
TREM2
downregulated in custer 13c
upregulated in custer 13c
HDAC9
FUT8
CX3CR1
ITGAM
P2RY12
APOE
FTL
FTH1
CD36
ABCA1
LPL
−log10 (adj. pvalue)
avg. log2 fold change

**Figure 7:**

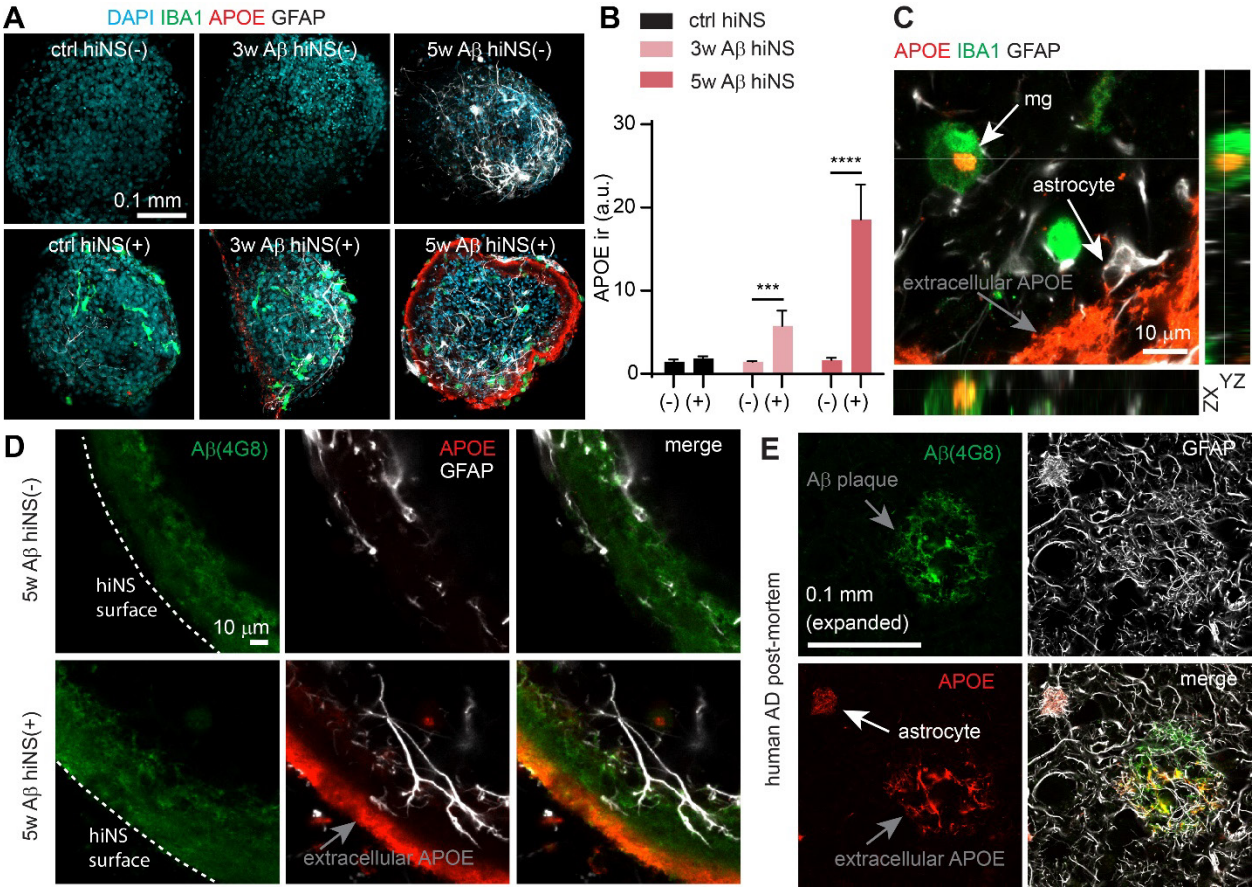
A
DAPI IBA1 APOE GFAP
ctrl hiNS(-)
3w Aβ hiNS(-)
5w Aβ hiNS(-)
0.1 mm
ctrl hiNS(+)
3w Aβ hiNS(+)
5w Aβ hiNS(+)
B
ctrl hiNS
3w Aβ hiNS
5w Aβ hiNS
APOE ir (a.u.)
30
20
10
0
***
****
(-) (+)
(-) (+)
(-) (+)
C
APOE IBA1 GFAP
mg
astrocyte
extracellular APOE
10 µm
YZ
ZX
D
5w Aβ hiNS(-)
5w Aβ hiNS(+)
Aβ(4G8)
APOE
GFAP
merge
hiNS
surface
10 µm
extracellular APOE
E
human AD post-mortem
Aβ(4G8)
Aβ plaque
GFAP
0.1 mm
(expanded)
APOE
astrocyte
merge
extracellular APOE